Mar Pérez Sar
Supervised by Josefa Becerra González

Universidad
de La Laguna

Searching for New Very High-Energy Blazars Candidates with Fermi LAT

March 2023
San Cristóbal de La Laguna
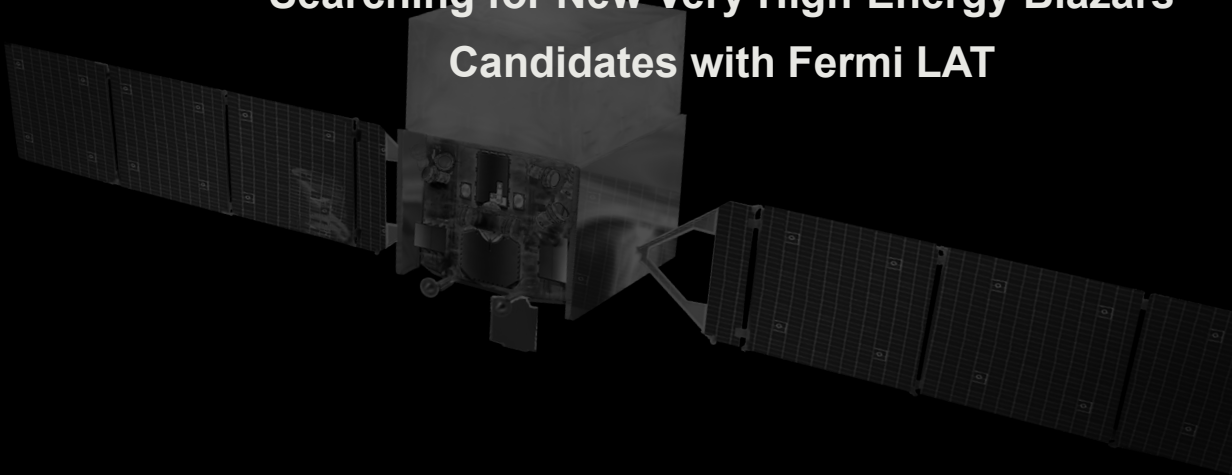
RESUMEN

La opacidad de la atmósfera, el bajo flujo de fotones y las altas energías que se ven involucradas en la astronomía de rayos gamma hacen de ella una de las disciplinas observacionales más desafiantes de la astronomía moderna poniendo a prueba tanto la capacidad tecnológica como creativa del ser humano. Los métodos actuales para la detección de rayos gamma son esencialmente dos: de forma directa a través de satélites como es el caso de Fermi-LAT y de forma indirecta a partir de los telescopios Cherenkov (IACTs en inglés) como CTA o MAGIC. Estas dos técnicas de observación se diferencian principalmente en el rango de energía en el que son sensibles y en la resolución angular que pueden alcanzar. Mientras los satélites pueden cubrir desde unos pocos MeV hasta varios cientos de GeV con una baja resolución angular, los IACTs son sensibles desde los GeV hasta varios TeV brindándonos precisiones angulares superiores. No obstante, existe otra diferencia fundamental y es que al contrario que los satélites, los IACTs no pueden hacer 'surveys' del cielo, limitados tanto por su pequeño campo de visión como por las condiciones en las que pueden observar. Esto hace que la selección de targets sea crucial para ellos y que ambos métodos acaben convergiendo y complemententándose.

El *objetivo* de este trabajo se sitúa en el punto de convergencia de ambos métodos y consiste en crear un catálogo de fuentes no detectadas previamente en el rango de muy altas energías que permita ampliar la familia de objetos a estudiar por los telescopios IACTs. En concreto nos vamos a centrar en blazares, ya que dominan el cielo extragaláctico en rayos gamma. Para ello, se hará uso de los 13 años de datos del satélite Fermi-LAT cubriendo desde el 4 de agosto de 2008 hasta el 5 de noviembre de 2021 en el intervalo de energía de 30 GeV a 2 TeV, lo que casi duplica la estadística de los dos catálogos de alta energía actuales de *Fermi*-LAT, el 2FHL y el 3FHL (Fermi-LAT Catalog of High-Energy Sources). La elección del intervalo de energía responde a que los detectores Cherenkov CTA y MAGIC en los que estamos interesados comienzan a detectar a partir de 30 GeV y 50 GeV respectivamente.

La *metodología* que se ha usado para la construcción de este catálogo consta de tres pasos: la creación de un mapa del cielo adecuado para nuestro caso científico, la implementación de un método de detección de fuentes de interés y, por último, el análisis individual de cada una de ellas desde el punto de vista de la detectabilidad por CTA/MAGIC.

Para la creación del mapa del cielo se han usado las llamadas 'fermitools', una serie de herramientas proporcionadas por la colaboración Fermi que permiten hacer cortes en energía y tiempo así como realizar el posprocesamiento de los datos proporcionados por el satélite. Posteriormente, se corre el algoritmo de identificación de fuentes en dicho mapa del cielo, detectando excesos de flujo. Esta primera identificación de lo que llamamos 'seeds' puede corresponder tanto a fluctuaciones estadísticas como a fuentes reales. Para discernir si se trata o no de una fuente real se realiza un test de significancia que, además de la TS, nos proporciona parámetros relacionados con el espectro. El algoritmo de identificación también asocia las fuentes encontradas con fuentes catalogadas en el catálogo de bajas energías de Fermi, el 4FGL DR3, ya que una fuente que consigue acelerar fotones a altas energías es probable que pase por energías intermedias no tan extremas. A continuación evaluamos si estas nuevas fuentes pueden ser detectadas por MAGIC y CTA. Para ello, utilizamos los parámetros espectrales derivados del estudio de significancia y extrapolamos la SED a los rangos de energía alcanzables por CTA y MAGIC. Mediante un sencillo algoritmo calculamos el factor que debe aumentar su flujo para que la fuente en cuestión sea detectable por cada uno de los instrumentos en 5, 15 y 50 horas de exposición. Finalmente, para tener una idea aproximada de si la fuente puede alcanzar dichos niveles de flujo, hacemos una estimación del flujo máximo que puede alcanzar. Con toda la información recolectada, construiremos un catálogo de nuevas fuentes en el rango de energía de 30 GeV -2 TeV, en el que se especifican tanto los parámetros espectrales como las condiciones de detectabilidad estimadas.

Este trabajo incluye también una sección en la que se evalúan las limitaciones y fortalezas de la metodología. Entre las limitaciones se analizará la confusión de fuentes, es decir, la posible asociación errónea entre un candidato identificado y su fuente 4FGL DR3 impuesta y la falta de estadística debido al bajo número de fotones que manejamos en este rango de energía. Por otro lado, entre los puntos fuertes encontraremos: los bajos niveles de ruido y aún más considerando sólo la región fuera del plano Galáctico ($|b| > 10°$), la buena resolución espacial, útil para el problema de confusión de fuentes, y finalmente la estadística. Pues si bien el número de fotones es pequeño, estamos casi duplicando los años respecto a los catálogos 3FHL/2FHL, pasando de 7 a 13 años.

Como *resultados* obtenidos, nuestro algoritmo nos ha proporcionado un total de 1741 'seeds' iniciales de las cuales se han analizado las 389 primeras (124 en el 4FGL DR3) en orden de flujo. Tras el estudio de significancia contamos con 90 candidatos potenciales entre los que se encuentran los siguientes tipos de blazares: BL Lacs (BLL), BL Lacs extremos (EXT), radiocuásares de espectro plano (FSRQ) y candidatos a blazar no clasificados (BCU). Tanto los EXT como los FSRQ son de gran interés para ser estudiados por IACTs. En el caso de los EXT esto se debe a que el rango de energía en el que su espectro es máximo no coincide con el rango en el que satélites como *Fermi*-LAT son sensibles por lo que detectarlos con IACTs hará que podamos estudiarlos con mucha más precisión. En cuanto a los FSRQs, su detección en rayos gamma supuso la caída de los modelos 'canónicos', los cuales no predecían que estos objetos fuesen capaces de acelerar fotones a tales niveles de energía. Aumentar la estadística de FSRQs es un objetivo primordial si queremos afinar nuestros modelos.

El documento está organizado en cinco partes. En la primera sección se ofrece una visión general de los conceptos teóricos tratados. Las secciones 2 y 3 se destinan a la descripción de la metodología empleada, así como al estudio de sus limitaciones y puntos fuertes. La sección 4 contiene los resultados y su discusión y, por último, en la sección 5 se presentan las conclusiones.

Contents

List of Figures

List of Tables

1. Introduction

Out of all the forms of electromagnetic radiation through which we can observe the Universe, gamma rays have been the most recently discovered. From the first detection of a cosmic very high energy (VHE) source in 1989 with the observation of TeV gamma rays from the Crab nebula, our eyes have witnessed the birth of a new era of discovery in which non-thermal phenomena reveal a violent and extreme Universe vastly unexplored. The great potential of this discipline comprises many of the riddles of modern astrophysics such as the origin of galactic and extragalactic cosmic rays, the mechanism of energy extraction from black holes, the processes of particle acceleration and radiation under extreme astrophysical conditions and even the possibility of a link with high-energy neutrino sources.

All this became possible thanks to space-born instruments in the high energy band (HE, E>100 MeV) and with ground based Cherenkov telescopes in the very high energy regime (VHE, E>100 GeV) where only of the order of ~ 80 VHE extragalactic sources (mostly blazars) have been discovered to date[1]. Apart from the energies that these two methods of detection can reach there is another fundamental difference between them. While space born telescopes as Fermi-LAT have a large field of view and can operate continuously, ground air Cherenkov telescopes operate in pointing mode due to their small fields of view and only during night time and good weather conditions, which makes the selection of targets crucial for them.

In this context, the aim of this work is to create a catalogue of new VHE blazars candidates, using data from the *Fermi*-LAT satellite, to extend the family of objects followed up by ground-based telescopes. Although not very sensitive to these energies, *Fermi*-LAT can take advantage of the low background levels in this regime and of the 13 years of collected data. This will almost double the statistics of the current high energy catalogs: 2FHL and 3FHL created from the first 7 years of the mission. Thus, the goal will be to discover new sources emitting HE photons, starting at 30 GeV, which will be the CTA energy threshold.
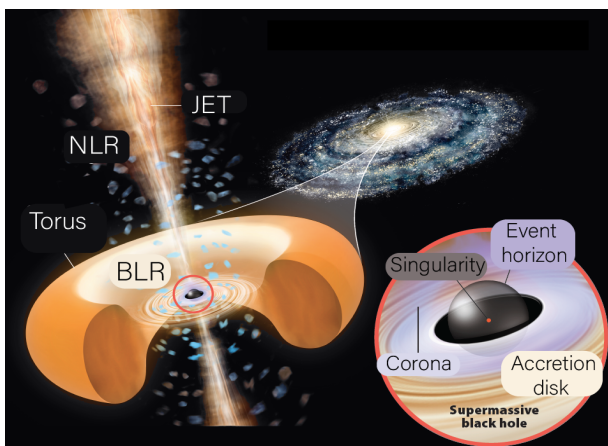

Fig. 1. Representation of the structure of an AGN. From inside out, AGN consist of a supermassive black hole; an accretion disk and a hot corona of gas; a fast-moving gas region, BLR; an obscuring torus of dust; and a slower-moving gas region, NLR. Credits: Roen Kelly

---

[1]http://tevcat.uchicago.edu/

1.1. Blazars within the AGN scheme

Active Galactic Nuclei (AGNs) emerge as powerful and persistent sources powered by accretion onto a supermassive black hole. From them, we receive a broadband spectrum that results from the interplay of thermal and non-thermal mechanisms involving different structures from sub-parsec to kilo parsecs scales. The most general picture of an AGN is shown in Figure 2 and could be structured as follows (1), (2):

- A central super massive black hole (SMBH) of typically $M_{SMBH} \approx 10^6 - 10^{10} \ M_\odot$.

- An accretion disk of diffused matter falling into the SMBH due to angular momentum losses. The disk extends from $\approx 10^{-2}$ pc to 10^{-3} pc and is believed to be purely thermal peaking in the optical-UV energy range.

- A X-ray corona close to the central object, probably caused by a population of electrons above the disk, which may take energy away from the SMBH when it rotates. The accretion disk photons can be scattered by hot material in the corona up to X-rays energies through inverse-Compton (IC) processes.

- Gas structures protruding with respect to the accretion plane that give rise to broad and narrow emission lines. The broad line region (BLR) is tipically at a distance of $d \approx 10^{-2} - 1pc$ and is believed to be formed by dense clouds of ionized gas with fast rotation speeds due to the influence of the central black hole gravitational potential. On the other hand, the narrow line region (NLR) is made of ionized gas of lower density and velocity. It extends far away from the SMBH up to ~ 10^{2-3} pc and it is under the influence of the host galaxy. The typical range of velocity widths are 1000-10000 km/s for BLR and 200-500 km/s for NLR. (3)

- A torus or warped disk located at $0.1 - 10$ pc away from the SMBH. The torus is expected to be within the gravitational influence of the SMBH and could be considered, in a broad sense, the cool outer regions of the accretion disk where molecules and dust grains can form. It is optically thick to optical/UV radiation so it can induce significant absorption and polarization of the radiation coming out from the central part (SMHB+disk+BLR) depending on the orientation of the structure with respect to the line of sight. This absorbed optical/UV light is then re-emitted in the infrared (IR).

- Host galaxy, which tipically can extend a few kiloparsecs, to over one hundred kiloparsecs in diameter. Its emission is associated with the thermal continuum of stellar formation and spans from the IR to OP bands.

- Relativistic jets, i.e, collimated outflows of energetic particles usually projected perpendicularly to the disk plane, with tangled magnetic fields that extends up to kpc scales beyond the host galaxy. Jets plow into the extragalactic medium and interact with surrounding matter. Then they are decelerated and can produce giant structures called lobes (4). The relativistic jets constitute the non-thermal emission of the AGNs covering most of the electromagnetic spectrum from radio to gamma rays and being the dominant part in
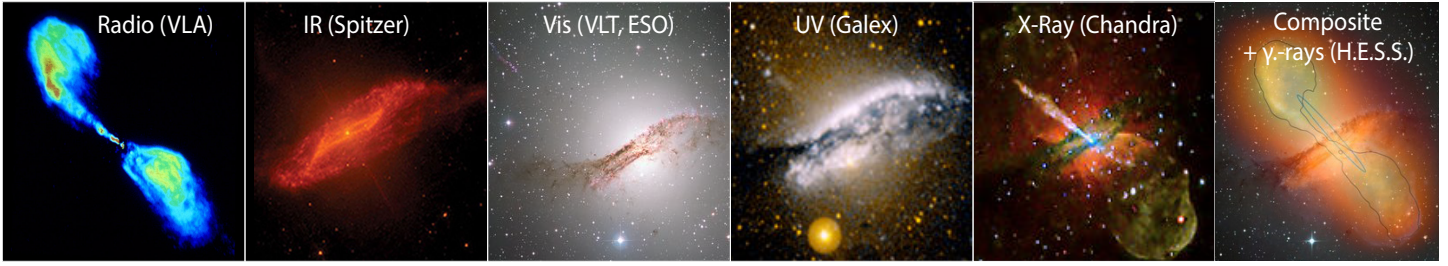
Fig. 2. Centaurus A, a radiogalaxy-type AGN as seen through different spectral windows. Centaurus A's dusty core is apparent in visible light, but its jets are best viewed in radio, X-ray and gamma-ray light. Credits: VLA/Spitzer/VLT/ESO/Galex/Chandra/H.E.S.S.

the spectral energy distributions (SEDs) of jetted AGNs[2].

As the number of discoveries increased, subcategories of AGN emerged and the idea of a unified scheme soon gained ground. This unified understanding proposed that the variety of features observed in AGN were derived from orientation effects, as the emitted light was influenced by various phenomena such as absorption, anisotropy, and beaming. Now it is widely accepted that these differences are not only caused by the observation angle but also by the source luminosity or black hole spin which are related with its accretion rate.

According to the accretion rate dependence we have two general flavours: radio-loud and radio-quiet AGNs. The main difference between them is the presence (radio-loud) or abscence (radio-quiet) of relativistic jets. On one hand, radio-loud objects are mainly hosted by giant elliptical galaxies and are believed to be generated by recent mergers since the coalescence of two similar-mass super massive black holes can result in a very massive rapidly spinning Kerr black hole, whose rotational energy and accretion can power a jet. Conversely, radio-quite objects are predominantly found in spiral galaxies or in mergers where the resultant spin is slow. The rest of the sub-classifications rely mostly on the observing angle. If an AGN is seen edge-on, the BLR is blocked by the dusty torus along the line-of-sight and only NLR can be seen from the observed. As we increase the angle, the BLR starts to become visible. When the AGN is seen pole-on, BLR and NLR may still be present, but they can be outshined by the jet emission if present.

In this work we will be focusing on blazars, radio-loud AGNs where the jet is aligned towards us. In the extragalactic gamma-ray sky, they represent the vast majority and exhibit rapid variability, high luminosities, and superluminal motion, which are consequences of the beamed emission from bulk relativistic motion of plasma along the jet.

1.1.1. Emission models

Blazars have a characteristic double-peaked spectral energy distribution (SED) that can extend from radio up to γ rays.

The lower energy component is normally explained as

synchrotron emission from ultra-relativistic leptons (electrons and positrons) moving along the jet in a tangled magnetic field.

For the high energy component, the origin of the radiation is more uncertain and two possible scenarios have been proposed: leptonic (the most established ones) and hadronic. (1)

- In the leptonic scenario, the plasma is dominated again by relativistic leptons (electrons and positrons) which undergo inverse Compton (IC) scattering. If the seed photons for the IC are the synchrotron photons of the low energy component (coming from the same population of leptons), the process is called Synchrotron–Self–Compton (SSC); if the main seeds are ambient photons produced externally to the jet (disk radiation, BLR lines, torus, etc.), the process is called external Compton (EC). (6) (7)

- In hadronic models, protons can also be accelerated to ultra-relativistic energies by a combination of proton synchrotron, π^0 decay and synchrotron and inverse Compton from secondary particles.
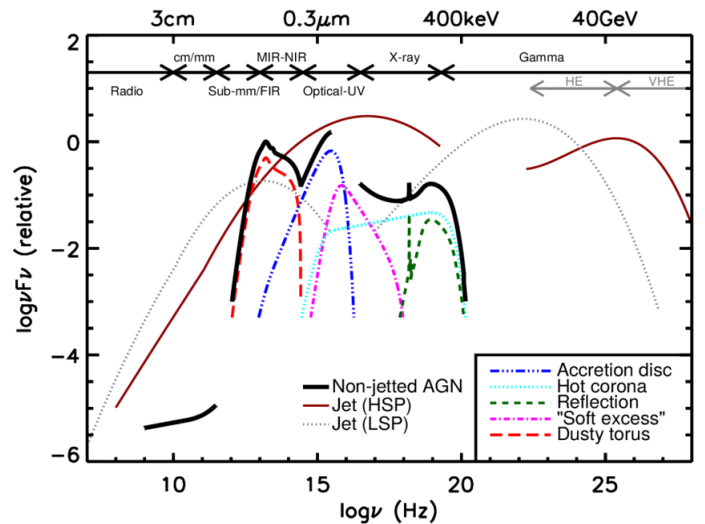
Fig. 3. Schematic representation of an AGN spectral energy distribution. Blazars corresponds to the jetted cases where the emission of the non-thermal component dominates. (8)

Yet neither of these scenarios is able to successfully explain some observations as for example neutrinos in leptonic models or fast (minute) variability in hadronic. Several alternatives have been proposed to address these problems including multi-zone emitting regions or structured jet models. However, more data

---

[2]The mechanism behind launching of the relativistic jets from the central part of the AGN is still hotly debated. Two leading theories were proposed in the 70s and 80s. Blandford and Znajek (1977) claimed that jets are launched by accretion disk through the process of electromagnetic extraction of energy and angular momentum from an accretion disk. Blandford and Payne (1982) suggested that jets are a result of the extraction of rotational energy from the spinning SMBH. (5)

and analysis is needed to test all these hypotheses. (1) (2)

As we previously mentioned, the bulk of these continuum radiation does not originate in the nucleus of the AGN but in the two jets that emerge usually symmetrically from the core and its origin is fundamentally non-thermal. However, some of these AGN have thermal components that can locally surpass the non-thermal double-peaked spectrum anywhere in the IR to ultraviolet band (Figure 3). Examples of these components are the IR emission from the dusty torus, the optical/UV emission from the accretion disk, the radiation from the X-ray corona and the emission lines arising from the NLR and the BLR. (2)

1.1.2. Absorption of γ rays

Once emitted, the very-high energy (>100 GeV) photons do not travel unimpeded through cosmological distances, but its propagation is limited by pair production processes. Their absorption can happen in the source scales, which we call self-absorption but also it can occur with the lower energy photons of the so-called extragalactic background light (EBL).

The EBL is the cumulative radiation emitted by all galaxies and other extragalactic sources throughout the Universe. This radiation includes ultraviolet, visible, and infrared wavelengths, and is thought to be composed of light emitted by star formation processes (star light and star light absorbed/re-emitted by dust), AGNs and may also contain diffuse and extended signals. The EBL is an important area of study as it holds valuable information about the history of star formation and galaxy evolution in the Universe. It provides insight into the number and types of galaxies that exist, as well as their luminosity and spectral characteristics.

The existing EBL intensity measurements are due to a combination of ground and space-based observations of the sky. However, the weakness of its emission make direct methods extremely challenging leading us to the exploration of indirect methods. A good example of one of them is the use of absorbed gamma-ray spectra of individual blazars and other AGNs at cosmological distances. These observations offer a mean of estimating the intensity of the EBL at the lower optical and IR wavelengths providing useful information on star and galaxy formation in the early Universe. (4) (9)

1.1.3. Blazar types

Blazars can be divided into two classes: BL Lac objects (BLL) and flat spectrum radio quasars (FSRQs). The classical division between FSRQs and BLLs was the presence or lack of strong optical emission lines, respectively, due to the presence or lack of the broad line region. Today, they are distinguished also by their accretion rates or jet powers, with higher accretion rate the FSRQs and lower-power the BLL. Blazars can also be sub-classified according to the position of its synchrotron peak: (i) low-synchrotron-peaked (LSP, $\nu_{SP} < 10^{14}$ Hz), (ii) intermediate-synchrotron-peaked (ISP, 10^{14} Hz $\leq \nu_{SP} < 10^{15}$ Hz, (iii) high-synchrotron-peaked (HSP, 10^{15} Hz $\leq \nu_{SP} < 10^{17}$ Hz) and (iv) extreme high-synchrotron– peaked (EXT, $\nu_{SP} \geq 10^{17}$ Hz). The LSP and ISP groups contain both BLLs and FSRQs, whereas HSPs are predominantly BLLs.

The detection of broad and faint emission lines in BLLs at high redshift prompted the idea that BLLs and FSRQ might be part of an underlying blazar sequence. Introduced in 1998 to attempt a first unified view of the broadband emission properties of blazars, the blazar sequence succeeds in describing the observed properties of blazars within a simple theoretical scheme in which the bolometric luminosity governs the appearance of the spectral energy distribution. However, the blazar sequence was and remains a hotly debated topic with the objection that it may be the result of selection effects operating not only when it was proposed, but even now, despite the presence of more sensitive instruments (6).

1.2. Detection of γ rays

As an observational discipline, gamma-ray astronomy has always been extremely challenging.

The extinction caused by the Earth's atmosphere makes satellites, as *Fermi*-LAT, the only means of direct detection of gamma rays up to tens of GeV. But above that energy threshold, this technique is no longer successful. The very low fluxes of cosmic gamma rays, combined with their high energy, require the construction of large and complex detectors that cannot be sent into orbit. Therefore, the hunt for VHE gamma rays returns back to ground with indirect methods of detection. We forget about the passage of the original gamma-ray photon to focus on the subatomic particles it generates when interacting with the nuclei of the atmosphere in a loop of pair production and bremsstrahlung processes. The resulting electromagnetic cascade is often referred to as an extensive atmospheric shower (EAS) and is composed of thousands of highly relativistic particles. (10)

Under normal conditions, the passage of a charged particle in the atmosphere polarises the medium symmetrically and the radiation contributions cancel out upon depolarisation. However, if the charge is faster than its own electric field (or in other words, if the speed exceeds the speed of the light in the atmosphere), the polarisation becomes asymmetric and so does the emitted radiation. The interferences no longer cancel and the contributions add up in a similar way as the superposition of the sound wavefronts when breaking the sound barrier (10). Instead of a wave shock, Cherenkov flashes of nanoseconds are produced in the blue/ultraviolet range that can be observed by the IACT (Imaging Atmospheric Cherenkov Telescopes) such as MAGIC or CTA.

In the following, we will briefly specify the basic performance principles of the instruments that we will consider in this work.

1.2.1. Fermi-LAT

The Large Area Telescope constitutes the primary instrument on the Fermi Gamma-ray Space Telescope mission from which we will take the data (hereafter we will call it *Fermi*-LAT). It is an imaging, wide field-of-view (FOV), high-energy γ-ray telescope, covering the energy range from below 20 MeV to more than 300 GeV, with good sensitivity down to tens of GeV. *Fermi*-LAT was built by an international collaboration and the bulk of the program is dedicated to a sky survey, in which the full γ-ray sky is observed every 3 h. *Fermi*-LAT is optimized
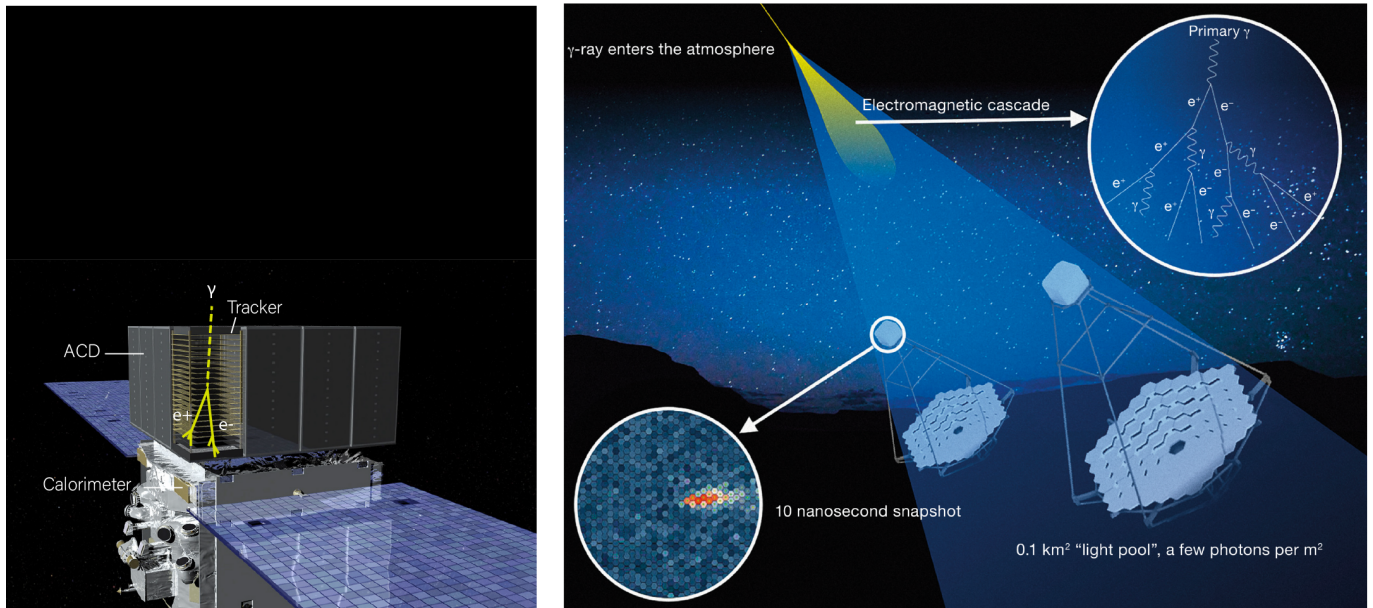
Fig. 4. (**Left**) 3D model of Fermi-LAT with its main parts. Credits: NASA (**Right**) Representation of IACTs performance when measuring an electromagnetic cascade created by a gamma ray. Credits: CTAO/ESO.

to produce a survey of the sky on timescales of months and to facilitate the monitoring and detection of variable and flaring γ-ray sources on shorter timescales. (11)

Its method of detection is based on the pair production principle and it includes four main detector systems: a tracker, a calorimeter, an Anti-Coincidence Detector (ACD) and a Data Acquisition System (DAQ). The tracker, in which the gamma rays interact by pair production, provides instrument triggering and determines the arrival direction of the detected photons. The calorimeter measures the energy deposition of the incident γ ray and generates an image of the electromagnetic shower development profile. The ACD surrounds the tracker and provides rejection of charged particles. And the data acquisition system performs onboard filtering in order to reduce the rate of background events that will be telemetered to the ground. (12)

1.2.2. Imaging Atmospheric Cherenkov Telescopes

The IACTs consist of a large segmented mirror that focuses the radiation onto a fast camera. Since a pulse of Cherenkov light lasts of the order of nanoseconds and they are extremely weak, the cameras must be sensitive to this light and use electronics and very fast exposures to capture it. Photomultiplier tubes (PMTs) are used to record and convert the light into an electrical signal, which is then digitized and transmitted.

The MAGIC (Major Atmospheric Gamma Imaging Cherenkov) telescopes, located in La Palma, have been exploring the sky at VHE γ rays (50 GeV – 50 TeV) since 2004, operating first with a single telescope and from 2009 with two telescopes in stereoscopic mode. Both have a diameter of 17 m, with a collection area of 236 m^2. The pointing system of the telescopes works really fast, so they can rotate to any orientation in the sky in less than 30 seconds for gamma-ray bursts.

The Cherenkov Telescope Array (CTA) is the next generation ground-based observatory for γ-ray astronomy at VHE. It will be capable of detecting γ rays in the energy range from

30 GeV to more than 300 TeV with unprecedented precision in energy and directional reconstruction. It will be located in the northern hemisphere at La Palma, Spain, and in the south at Paranal, Chile.

Telescopes of several sizes are build in order to optimize different energy ranges. The higher the energy of the γ ray, the larger the number of interactions and the larger the cascade size. MSTs (medium-sized telescopes) are the most similar in diameter to the current generation of IACTs, around 12 m in diameter, and they are optimized in an energy range between 150 GeV and 5 TeV. They will improve the current sensitivity of IACTs by an order of magnitude, and their large FOV (7.6 degrees) will allow to perform scans of large parts of the sky. The arrays of four LSTs (large-sized telescopes), with 23 m diameter reflectors, will allow to extend the IACT technique into the still-poorly-exploited region of tens of GeV where the ellipse of the particles shower can be traced by just one or fewer telescopes. Finally, the SSTs (small-sized telescopes) will be large (70 units) arrays of telescopes of a few meters in diameter ($\sim$4 m) and wide FOV ($\sim$8-10 degrees). They are aimed at providing optimal sensitivity, angular resolution and surveying capabilities at energies of tens of TeV, i.e, for the biggest cascades sizes. (13) The northern hemisphere network will be composed of 4 LSTs and 15 MSTs, covering a total area of approximately 0.6 km^2 and an energy range from 30 GeV to more than 20 TeV. Its main goal will be the study of extragalactic sources at the lowest achievable energy. The southern hemisphere network will consist of 4 LSTs, 25 MSTs and 70 SSTs, covering an area of 4 km^2 in the whole energy range from 30 GeV to 300 TeV. It will reach such high energies because it is intended to focus on the study of galactic sources, which can emit at extreme energies and which are not affected by the absorption of the EBL. (14)

2. Methodology

Three main phases can be distinguished in the creation of a catalog. The first one is the construction of a sky map suitable for our scientific case. The second, the implementation of a detection method for the sources of interest. And last one, the individual analysis of each one of them. In this section, we will review these three key levels in order to have a proper vision of the global process.

2.1. Data

We use 13 years of data from *Fermi*-LAT covering from 2008 August 4 (15:43 UTC) to 2021 November 5 (17:35 UTC) in the interval of energy from 30 GeV to 2 TeV. With this, we almost double the statistics of the two currently high energy catalogs, the 2FHL and the 3FHL, having the opportunity to discover sources that are not yet detected in this regime. The choice of the energy interval responds to the desire to provide a reservoir of candidates to be followed up by Cherenkov detectors such as CTA or MAGIC, which start detecting at 30 GeV and 50 GeV respectively.

Table 1. Differences between previous catalogs and the one presented in this work

	T_{start}	T_{end}	Energy
2FHL	04/08/2008	01/05/2015	50 GeV - 2 TeV
3FHL	04/08/2008	02/08/2015	10 GeV - 2 TeV
4FGL DR3	04/08/2008	02/08/2020	50 MeV- 1 TeV
4LAC DR2	04/08/2008	02/08/2016	50 MeV- 1 TeV
This catalog	04/08/2008	05/11/2021	30 GeV - 2 TeV

Notes. Both 2FHL and 3FHL are focused on the first 7 years of detection of *Fermi*-LAT while this catalog includes almost the entire telescope's livetime. We include the 4FGL DR3 catalog which we will use to associate new high-energy sources with their lower energy counterpart and the 4LAC from which we will get the redshifts.

The utilization of *Fermi*-LAT data is not straightforward and a selection of tools (`Fermitools`) needs to be understood in order to obtain a suitable sky map for our subsequent analysis. When talking about the *Fermi*-LAT data, we are talking about *events*, the result of the response of the detector to a photon, a charged particle, or a noise that mimics a particle. A detection depends both on the instrument hardware and on the event reconstruction algorithms that calculates the event parameters from observables and assigns probabilities of being or not the result of a background fluctuation. The global result of the performance gives rise to the Instrument Response Function (IRFs), which depends on the efficiency in terms of the detector's effective area, the resolution as given by the point-spread function (PSF) and the energy dispersion.

Photon and spacecraft data were downloaded directly from the Fermi Science Support Center web site (15). The photon files include the events with their energy and information about the quality of the event reconstruction. The spacecraft file has information about the pointing and livetime history of the instrument.

Data selection We use `gtselect` to make the temporal and energy cuts, in addition to other types of filtering such as event class, event type and maximum zenith distance for which events

are kept[3]. Event classes are subsets of events selected in terms of the probability of being photons. Higher probabilities imply smaller effective areas, narrower point spread functions (PSF) and lower contamination of background events. Each event class has a corresponding set of response functions that are unique of that class. The response functions for each class are internally partitioned into 3 'event types': FRONT/BACK conversion which tells us whether the event has been detected in the Front or the Back section of the Tracker[4]; PSF, which indicates the quality of the reconstructed direction; and EDISIP, related with the quality of the energy reconstruction.

Following the data selection recommendations we chose SOURCE class (evclass=128) and FRONT/BACK for event type (evtype=3). More restrictive classes such as CLEAN or ULTRACLEAN are designed to have 2-4 times lower background rates, but this could led to a poor result in our objective of searching for new sources, since only the most powerful ones would appear in the map. At the time of this thesis *Fermi*-LAT was in the 8 data release (*Pass 8*) so the IRF used was $P8R3\_SOURCE\_V3$ according to the class and type of our events.

Once our data is selected, we use `gtmktime` to make cuts based on the parameters on the spacecraft file to defined the time ranges where the data is considered valid, i.e, in which *Fermi*-LAT was properly working and collecting data. For example, *Fermi*-LAT does not collect data while transiting the Southern Atlantic Anomaly or during rare events such as software updates, spacecraft maneuvers or solar flares. Thus, we update the previous selected data and bound it to the called good time intervals (GTIs).

Count map In order to identify clusters of photons expected from the sources, we use `gtbin` which can provides us with a count map in one energy band (CMAP option) or multiple energy bands (CCUBE option). In this work we construct two different maps using both modes. The first one has only one bin of energy and will be the one used to identify the sources and a second one divided in 5 bins to determine how the photons of the identified sources are distributed in terms of energy.

Exposure map The exposure map is defined as the total exposure (effective area multiplied by time) weighted by the total IRF, which depends on the inclination angle (the angle between the direction to a source and the instrument normal). Thus, the number of counts that a source produce depends on the amount of time that it spent at a given inclination during an observation.

Calculating the exposure first requires calculating the instrument livetime for the entire sky (using `gtltcube`) using the good time intervals to compute the time the instrument has spent at each position as a function of the inclination[5]. Then

---

[3]Photons coming from the Earth limb are a strong source of background and a $z_{max} = 90$ is suggested for reconstructing events above 100 MeV

[4]The response is different since a multiple-scattering is more likely to occur in the thicker material of the back part resulting in a worst angular resolution.

[5]We use the standard good time interval filter $DATA\_QUAL = 0$ and the recommended instrument science configuration $LAT\_CONFIG = 1$ for the gltcube computation

we convolve the livetime with the IRF (using `gtexpcube2`), obtaining the exposure at each point in the sky in each energy bin.

Flux map. We use `farith` which is part of the `HEAsoft package`, to compute the flux map by dividing the count map by the exposure map. Then, we can normalize the map for visualization purposes.

It is worth noting that even if we compute the entire sky map, we won't take into account the 10 degrees that surround the galactic plane ($|b| \leq 10^o$). This allows us to avoid both the high density of objects of the Galactic plane (which can pose a computational problem when identifying seeds) and the biggest part of the contribution of the Galactic diffuse emission[6].

The resultant maps (Flux and energy-binned sky-maps) have a dimension of [3600,1800] pixels. Each pixel are square and 0.1^o wide, i,e, we have a 0.1 degree spatial bins. The maps are in galactic coordinates and with an AIT (Hammer-Aitoff) projection.

2.2. Source Detection

Once we have our sky map, 'seeds' of sources are identified via a sliding-cell algorithm as excesses above the background of clusters of 2 or more photons. This list may include statistical fluctuations as well as real sources. A maximum likelihood study is then performed in order to verify which, among the seeds, are the reliable sources.

2.2.1. Source Identifier Algorithm

The nature of the algorithm is rudimentary but responds to an ingenious way to automate rapid source identification across the entire sky map. Figure 5 displays the four steps in which this simple algorithm operates, which is somewhat reminiscent of the 'tip tap toe' game.

First step. The algorithm scans the sky map ($|b| > 10°$) and reads the values of each pixel. Then, it takes as seeds the pixels that exceeds a given threshold ($F_{threshold}$ = 1.21 which was found to correspond to points with at least two photons). After this, we have a geometric network of points that discriminates areas with high density of counts as well as some random events. At this point, what we have is a lot of artifacts inherent to the geometry of the map since the algorithm is not sampling sources but pixels. The second step eliminates seeds on a geometrical basis too. For a given pixel asses whether exists a consecutive pixel in the same row that is also above the threshold. If this is the case, they are assumed to be part of the same event and the one with the highest flux stays. If not, they are considered independent seeds. The third and fourth steps are equivalent. They look for consecutive pixels that are above the threshold and select the one with higher value. The only difference is that the third step compares vertical pixels and the fourth, the diagonals. Thus, we only keep the seed in the position that enclose the maximum flux value within a possible source. In the case that we have a two nearby seeds but they are not connected by pixels above the threshold, they are considered
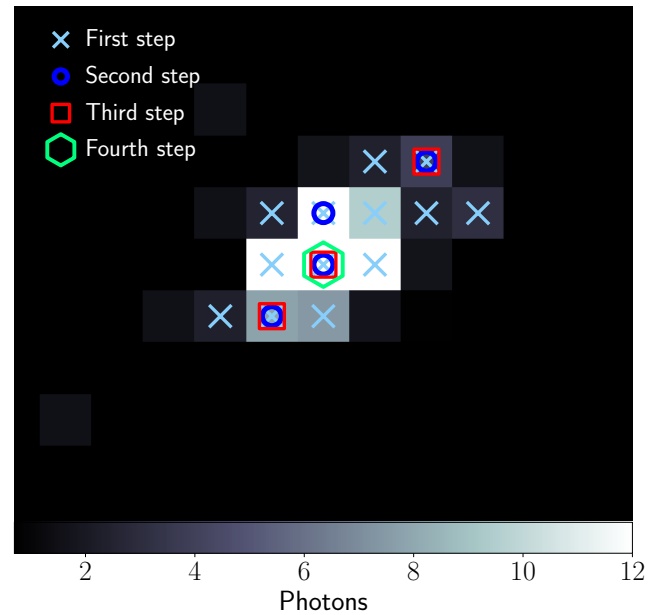
Fig. 5. Identification of seeds by our algorithm. `First step` identifies all pixels above a certain threshold. `Second step` chooses the pixel with highest value in the same row. From the ones remaining, `third step` chooses the pixel with highest value in the same column and analogous in the `fourth step` for diagonals.

as independent events.

Starting with 3768 seeds in the step 1, we reduce the sample by a 19% with step two, a 25% with step three and a 31% with the last one. We remain with a 69% of the initial seeds found.

The next step is associate the seeds with existent sources. We discard those already detected in the 2FHL and 3FHL catalogs. Remember that our purpose is to find new high energy candidates. The presumed new sources will be also contrasted with the 4FGL DR3 catalog for a possible counterpart match. These associations are made based on close positional correspondence (we impose a radius of 2 pixels, equivalent to 0.2°). The two main parameters on which the algorithm depends on are:

- The radius of association 0.2°[7].
- Limit of detection (F=1.21, 2 photons)

The first has been refined based on trial and error with obvious cases and the second has seemed to be a good limit based on the number of photons that we have in these energy ranges and what has been done by other catalogs. (17)

Finally, we may encounter two difficulties in our identifications (Figure 6). We can have the situation that within a 0.2° the seed can match two outcomes in 4FGL DR3. In this case we simply keep the one that is closest to our position. The second problem is what we have called 'duplicates', seeds found near detected sources and of which there is a reasonable doubt whether they are independent sources or belong to the nearby one. This case of study will be detailed later.

---

[6]Most of the diffuse emission is associated with γ rays produced by the decay of neutral pions, π^0, generated in collisions between cosmic rays protons and nuclei and the interestelar gas. (16)

[7]In the code it is not a radius but a square centered on the source with side 0.4° (which would be roughly equivalent to a radius of 0.2° except at the vertices where it can extend to 0.28°)
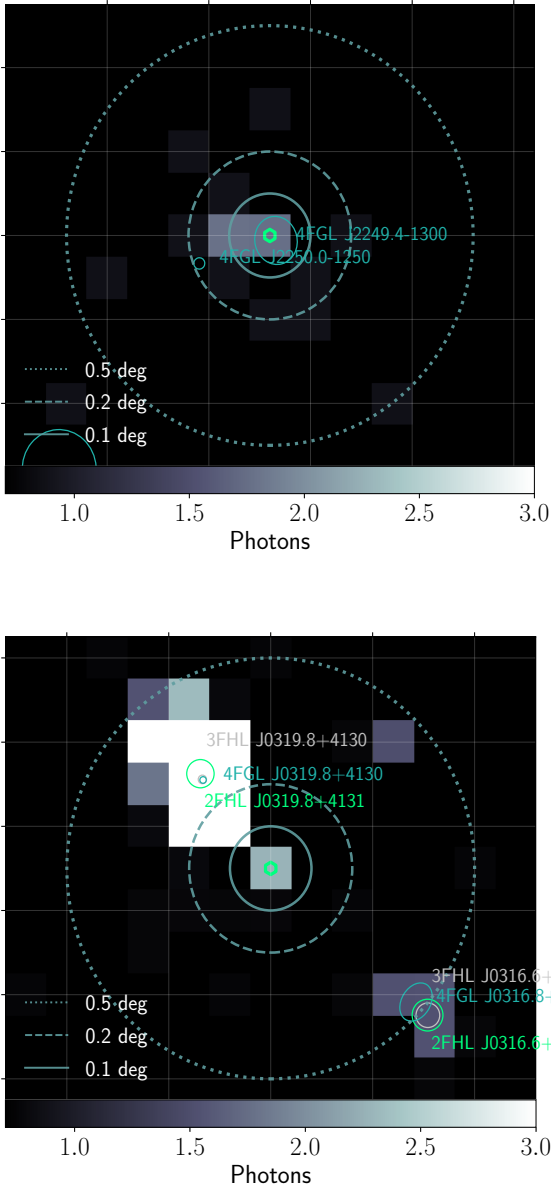
Fig. 6. Example of two difficulties faced in the association of sources with catalogs (white for 3FHL, light green for 2FHL and dark green for 4FGL DR3). Three radius centered on the source are defined to give an estimate of the distances. **(Top)** A seed can be associated with two sources in the 4FGL DR3 catalog under the criteria of an association radius of 0.2°. **(Bottom)** A seed can be associated with a nearby source despite not being within the defined 0.2° association radius.

2.2.2. Significance Tests

Even if a qualitative exploration of the data can suggest the presence of sources by the spatial clustering of photons, a quantitative analysis requires a significance test.

The significance is the probability that the excess in flux or counts in our map cannot be explained by background fluctuations alone. In astroparticles, we define a detection when the probability of the called null hypothesis[8] is less than 0.1%. This would correspond to a 5σ.

The *test statistic* for a point source is defined as (18):

$$TS = -2(ln\mathscr{L}_{max,0} - ln\mathscr{L}_{max,1}) \quad (1)$$

where $\mathscr{L}_{max,0}$ is the maximum likelihood value for a model without the source (null hypothesis) and $\mathscr{L}_{max,1}$ the maximum likelihood value for a model with the source.

In the limit of a large number of events (in our case photons), N, Wilks' Theorem states that the TS is asymptotically distributed as a χ_k^2 distribution, where k is the number of degrees of freedom (19). This means that if the null hypothesis is true then the observed and expected data will be close in values: $\chi_k^2 \approx 0$ and so the TS.

$$\chi^2 = \sum \frac{(O_i - E_i)^2}{E_i} \quad (2)$$

where O_i are the observed values and E_i the expected ones. Remember that with the null hypothesis we expect only background fluctuations. So a $\chi^2 \approx 0$ would mean that the source is compatible with noise.

In contrast, a large TS would indicate that the null hypothesis has a low probability of being true and that with high probability there is an actual source that can be quantified. A TS = 25 would correspond to a 5σ detection for $k = 1$. For higher degrees of freedom (as in our case $k = 2$), TS is still asymptotically distributed as a χ_k^2, but TS = 25 would not correspond to exactly 5σ but something in between 4σ and 5σ. According to (20),(21),(22) would be $\approx 4.8\sigma$.

Our criteria in this work is $TS \geq 16$ and $N_{pred} > 2$ for seeds that are associated with 4FGL DR3 sources and $TS \geq 25$ and $N_{pred} > 3$ for seeds that doesn't have an association in 4FGL DR3 catalog.

Maximizing the value of TS implies maximizing the likelihood function $\mathscr{L}$, which gives us the probability of reconstructing our data given an input model. Mathematically, it is the product of the probability of obtaining the expected counts for each pixel.

$$\mathscr{L} = \prod_{ij} p_{ij} \qquad p_{ij} = \frac{N_{pred}^{ij} e^{-N_{pred,ij}}}{n_{ij}!} \quad (3)$$

where p_{ij} is the Poisson probability of observing n_{ij} counts in the pixel ij when the number of counts predicted by the model is $N_{pred,ij}$. If we take the logarithm of the likelihood:

$$ln\mathscr{L} = \sum_{ij} n_{ij}ln(N_{pred,ij}) - \sum_{ij} N_{pred,ij} - \sum ln(n_{ij}!) \quad (4)$$

where we neglect the last term since is independent of the model. The first term makes $ln\mathscr{L}$ to increase if the model predicts counts in pixels where they actually occur while the second demands those counts to be precisely allocated (18). We can see that maximizing the likelihood is a great method for parameter estimation.

---

[8] The null hypothesis claims that the observed differences are due to chance, i.e, that the excess in flux that we observe is only due to noise.

In our case, the likelihood function would be the integral of the source model with the IRF evaluated at the observed direction, energy and arrival time of each photon.

$$ln\mathscr{L} = \sum_j M(E_j, \hat{p}_j, t_j) - N_{pred} \qquad (5)$$

Since the number of events is expected to be small in this energy range we use the unbinned likelihood analysis which is generally more sensitive as it considers each event separately with its own IRFs. For each source we need to run the steps explained in the Data Section, with the difference that we are not considering the whole sky anymore but only a ROI centered in our source. Then we need to compute the following steps.

Creation of a source model The `XML` source model for maximizing $\mathscr{L}$ will contain all the sources that are expected to exist in the ROI but also takes into account more distant ones that could have a contribution to the counts at lower energies due to a broad PSF. For 30 GeV *Fermi*-LAT has a PSF of θ_{68}[9] $\approx 0.15°$ decreasing even more at higher energies so the fact that these contributions could be important seems unlikely. However we choose a ROI of $2°$ (6 times the PSF) around each source and a larger region for the sources that can contribute up to $10°$ because with this we would take into account a larger number of photons to model, N, which would increase the statistical reliability of the study according to Wilk's Theorem.

For each one of the sources we have spectral and spatial information. But only the spectral parameters will be set as free in the fit.

In general, the spectral shape for our source is set to be a Log Parabola to account for the possibility of curved spectra types. However, at these energy intervals we will not have enough photons to detect curvature, so the spectrum can be associated with a Power Law or in other words a Log Parabola with $\beta = 0$. The expression for a Log Parabola is the following one:

$$\frac{dN}{dE} = F_0 \left(\frac{E}{E_b}\right)^{-(\gamma+\beta log(E/E_b))} \qquad (6)$$

where F_0 is the normalization flux, γ is the spectral index at the pivot energy E_b and β measures the curvature of the parabola. In this model, the energy is fixed to $E_b = 30\,\text{GeV}$ which is supposed to be in the bow tie region where the error in the estimation of the flux is minimum.

The spectral and spatial information of all the sources are retrieved from the 4FGL DR3 catalog through the program `make4FGLxml.py` (20). In case a source is not in the 4FGL catalog, we established the spatial coordinates encounter by our algorithm and for the spectral parameters we select standard values: $F_0 \subset (0, 10^6) \cdot 10^{-13}$, $\gamma \subset (1, 5)$, $\beta \subset (-5, 10)$ and $E_b = 30\,\text{GeV}$. The only parameters that are allowed to vary are the photon index, γ, and the normalization flux F_0 (i.e two degrees of freedom). For the rest of the objects, if they are in the ROI then its photon index and normalization factor are also free for the model fitting. If they are in the wider region of $10°$ then the spectral parameters remain fixed at the values offered by the 4FGL DR3 catalog.

The `XML` also includes the backgrounds from the galactic and extragalactic diffuse emission with the templates `gll iem v07.fits` and `iso P8R3 SOURCE V3 v1.txt` respectively. For both, we allow the normalization flux to vary in the fit.

Computation of the diffuse source response. As we previously mentioned the function that we want to maximize, is defined in terms of the expected photon distribution for a given source model. That distribution is the convolution of the source model with the instrument response which for an individual photon is computed as the integral of the source model with the instrument response evaluated at the observed photon direction, energy and arrival time. For point sources, the spatial component is a delta-function, so this integral is relatively easy to do but for diffuse sources such as the Galactic interstellar component, this integral is very computationally intensive. We use `gtdiffrsp` to precompute the expected contribution of the background diffuse sources for each event. In the likelihood calculations, it is assumed that the spatial and spectral parts of a source model factor in such a way that the integral over spatial distribution of a source can be performed independently of the spectral part and in this case the integral over the instrument response can be precomputed for each diffuse model component. (23)

Likelihood fit. Finally, we perform the likelihood fit. The `gtlike` tool provides for each source the best fit for the free parameters that we include in the `XML` model. The optimizer used in this work is `NEWMINUIT` and founds the maximum by iteratively calculate the function, $\mathscr{L}$ for different sets of trial parameters. By estimating derivatives of the function with respect to the parameters, the algorithms choose new trial parameters that are progressively closer to the set that maximizes $\mathscr{L}$, until the change in the function value between iteractions is sufficiently small (or the number of iterations reaches a maximum value). While iterating, the dependence of the function on the parameters is mapped out, particularly near the function's maximum. This is how the uncertainties are calculated. The end results is an output `XML` model with the best-fit values. It reports six parameters: F_0 ($MeV^{-1}\,cm^{-2}\,s^{-1}$), γ, β, N_{pred}, a TS value and the integrated photon flux above 30 GeV ($ph\,cm^{-2}\,s^{-1}$) (24).

The parameter space can be quite large since the spectral parameters from a number of sources must be fit simultaneously together with the diffuse components too.

The optimizers find the best fit spectral parameters, but not the location. The vast majority of the cases the new identified sources are already detected in the lowest energy catalog 4FGL DR3 in which positions are well determined. For those that do not have an associated 4FGL source, a deeper study should be made in terms of position determination, but this is not implemented in this work.

2.2.3. TS maps

As we have seen, there are some cases where the identified seed has no associated 4FGL source whitin a $0.2°$ radius but it is in the proximities of a powerful one (Figure 6). In those cases, where the nature of the photons is doubtful, we build a TS map.

---

[9]θ_{68} is defined as the half-angle of a cone that contains 68% of the events from a point source at a specific energy.

The tool `gttsmap` allows us to perform a grid search, that computes a TS value for each pixel of the map. The input is the source model centered on the 4FGL object near to our presumed 'New Source'. We assume a radius of 1° around it. The tool will make a fit of the source model and return us a residual map in which we can search for traces of the new candidate.

2.3. Individual analysis: SED and CTA/MAGIC Detectability

Once we have our catalog, we use the `SED Builder` tool from the Space Science Data Center (SSDC)[10] (21) to study the characteristics of each source, attending mainly to the type classification. A great majority of the sources are already classified in the 4FGL DR3 catalog but in some of them a subtype can be seen. In addition, the SEDs allow us to understand the characteristic features of each type of blazar, giving us a glimpse of the different scenarios of γ-ray emission.

We conclude this work assesing whether this new high energy sources can be detected by MAGIC and CTA, using the `SED extrapolation Fermi CTA.py` code written by Josefa Becerra (supervisor of this work). In this program, we can use the spectral parameters derived from the TS study and extrapolate the SED to the energy ranges achievable by CTA and MAGIC from 30/50 GeV onwards. Through a simple algorithm we manage to calculate the factor that the flux need to increase in order to trigger a detection in each of the instruments, for the time spans: 5 hours, 15 hours and 50 hours of exposition.

We will end up with a catalog in the energy range of 30 GeV -2 TeV, in which both spectral parameters and detectability conditions are specified for a group of new high energy sources.

3. Limitations and strengths of the methodology

3.1. Limitations and how we cope with them

The limitations of this work are mainly two:

- The source confusion, that is, the possible erroneous association between an identified seed and its imposed 4FGL DR3 source.

- The lack of statistics due to the low number of photons at this energy range.

Both of these problems are faced by every catalog in the VHE regime. Here we will compare how real catalogs deal with them and how we do it here.

3.1.1. Source confusion

In the *Fermi*-LAT catalogs, it is frequent to see the distinction between association and identification. Association is linked to spatial coincidence/position compatibility while identification is only firmly established on a timing characteristic such as periodicity for a pulsar or a binary; or a variability correlation with observations at other wavelengths (25) . This doesn't mean that every source in the 4FGL DR3 catalog meet the condition of identification. Thus, they developed two additional association techniques: the Bayesian and the Likelihood Ratio method. The Bayesian method assesses the probability of association between

a γ-ray source and a candidate counterpart taking into account the position uncertainty of the γ-ray source and the local density of possible candidates; this local density is estimated simply by counting candidates in a nearby region of the sky. Higher the density, higher the probability of a fake association. Conversely, the likelihood-ratio method makes use of surveys in the radio and in X-ray bands in order to search for possible counterparts among them. The procedure is similar to the Bayesian approach but the density of "competing" candidates is the density of sources that are at least as bright and have spectra at least as flat as the source[11] (26).

Even if these two methods are clearly more tuned and accurate that ours, we can still test the performance of our algorithm and assess whether the risks we take are scientifically solid. For this, we reconstruct the original sky maps used in the 2FHL and 3FHL catalogs and run the source identification algorithm on them. All sources of both 2FHL and 3FHL catalogs are identified, with the exception of those located in the galactic plane (see Figure 7).
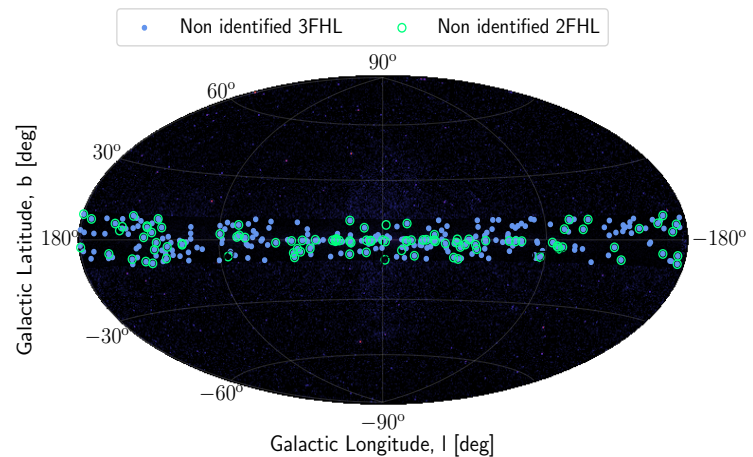
Fig. 7. Sources non identified by the algorithm in the 2FHL/3FHL maps. The sources non identified are located in the galactic plane, region avoided by the algorithm. The rest of the sample is fully reconstructed for both cases.

In the case of the 2FHL, 352 sources were identified from which 94 were duplicates. Thus we end up with 258 sources at $|b| > 10°$. For the 3FHL catalog, 1844 sources were identified with 605 duplicates. Then, we end up with 1239 at $|b| > 10°$. Remember that a duplicate is the case where two independent seeds are related to a same source either because it is a background fluctuation, a nearby independent source or a poor identification of the algorithm. This is not usually a problem since when we run the significance test, most of the duplicates are discarded and those that are significant enough are evaluated afterwards trough a TS map, as explained in the previous section.

We could also quantify the error we are making in the source association. In Figure 8 (left) we can see the distance separation between associated sources for the catalogs 3FHL, 2FHL (in their respective original sky-maps) and 4FGL DR3

---

[10]SSDC collects spectral data from numerous surveys across the electromagnetic range for a large number of sources throughout the sky.

[11]Some sources only comply with one of the methods. In other there are contradictions between the two methods and the one that yields less uncertainty remains.
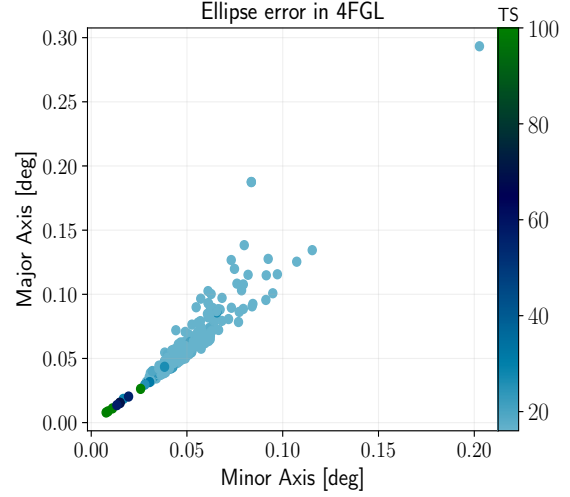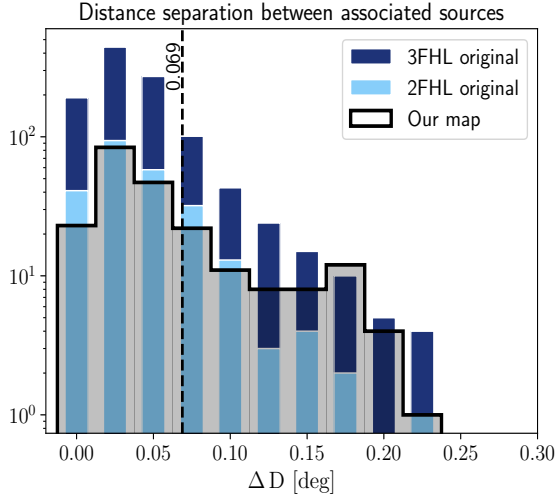
Fig. 8. (**Left**) Difference in the position determined by the algorithm and the correspondent associated source for three sky-maps/catalogs. In the case of this catalog, we contrast with the 4FGL DR3. (**Right**) Position uncertainty in 4FGL DR3 as a function of the TS for the associated sources detected in this catalog.

relative to this catalog. This histogram must be taken with care since this is partially biased by the radius of association that we imposed. However we can see that the tendency is closed to zero (which will happens even if we impose a larger radius within the reasonables ones) and falls visibly beyond that. In the case of the algorithm applied to this catalog we see a little bump around 0.175 but nothing really remarkable. On average the associated sources in the 4FGL DR3 are at a distance of $0.07°$ from the seed that we have identified.

If we now compare this with the typical errors in the 4FGL catalog (Figure 8, right panel), the vast majority of the sources that we are studying have a uncertainty below $0.10°$ in the 4FGL DR3 catalog. This makes our $\Delta D \approx 0.07°$ compatible with the 4FGL DR3 position errors.

3.1.2. Statistics

Statistics is the second big challenge of a study like this since particle (and photon) fluxes decrease rapidly with energy, due to the inherent difficulty of their acceleration[12].

Figure 9 shows the number of sources that have a certain number of photons as a function of energy. We represent the sources catalogued in 3FHL/2FHL evaluated both in their original sky-maps and in ours (labeled as updated). For the 3FHL catalog this implies a shift to higher energies, so the number of photons is expected to decrease, while for 2FHL the shift is to lower energies and conversely we will have more photons.

We can perceive that the catalog of this work has a much more peaked distribution in general, centered in lower numbers of events. This is because we are looking for sources not detected by the 3FHL/2FHL catalogs so it makes sense that the footprints of these remaining sources are fainter. From our sample of 1741 identified seeds only 91 have more than 3

photons, the rest have only 2^{13}.

In the 2FHL catalog the selection criteria for a source is that $TS \geq 25$ and $N_{pred} > 3$ (minimum number of events predicted by the model) while in 3FHL $N_{pred} > 4$. In our case we will see that only 2 sources are below $N_{pred} < 2$. They will be indicated in the corresponding tables.
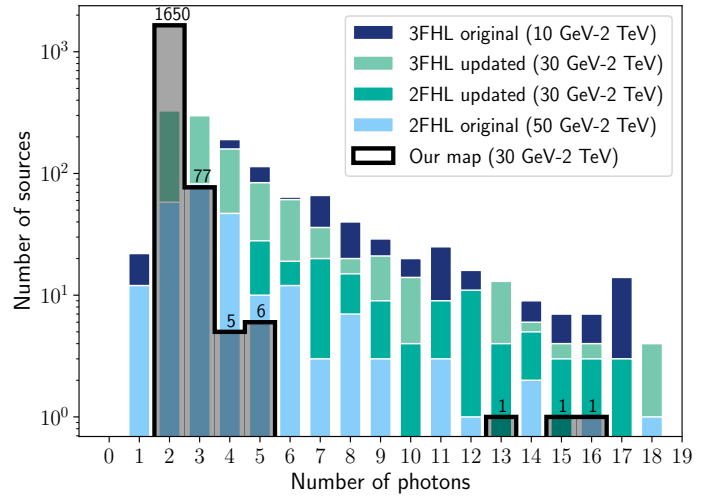
Fig. 9. Number of photons of catalogued sources from 3FHL/2FHL in their original sky-maps and in ours (30 GeV -2 TeV). In a black shade we display the new source candidates found in this work.

Even when dealing with a low number of photons, one have to bear in mind what is the energy of that photon, since the higher the energy the less likely it is to be a background fluctuation. Besides, the low background levels that we have in this energy range allows us to not need a large number of photons to still have valid significance tests.

---

[12]Acceleration of charged particles is a long standing problem in Astrophysics and still today the particular processes taking place are not well understood.

[13]This corresponds to the lower limit imposed on the identification algorithm.
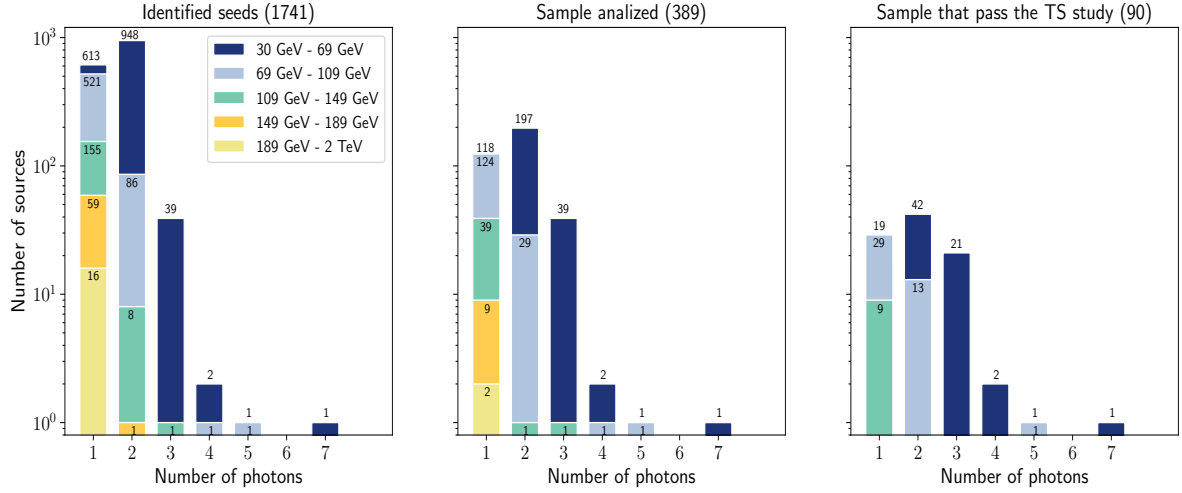
Fig. 10. Distribution of the photons of this catalog in 5 different energy bins through the different stages of the study.

In Figure 10 we can see how the photons of our sample are distributed in 5 bins of energy ranging from 30 GeV to 2 TeV. From left to right we display several stages of this study. We start with 1741 identified seeds but due to time constraints only 389 were analyzed through a significance test. The order of analysis is given by flux.

Again we can see that the amount of photons drops with energy bin. But it might seems curious why some of the considered 'reliable' photons for being in the most energetic bins (represented in yellow) have not pass the significance test. This is because these cases correspond to new sources not associated with the 4FGL DR3 catalog where the conditions to pass the test are more strict ($TS > 25$ and $N_{pred} > 3$) than for the others ($TS \geq 16$ and $N_{pred} > 2$).

3.2. Strengths

The assets of this work are the ones that make us address the aforementioned limitations.

- Low background levels and even more since we are considering only the region outside the Galactic plane ($|b| > 10°$). This helped us in terms of statistics since we don't need a large number of photons to still have valid significance tests.

- Better spatial resolution, useful for the source confusion problem. For 30 GeV, $\theta_{68} \approx 0.15°$, roughly the width of one of our pixels.

- Statistics, again. Even if we are lowering the photons, we are doubling the years compared to the 3FHL/2FHL catalogs, going from 7 years to 13. This is the key in the hunt of new VHE sources.

Figure 11 captures the idea of this section: the trade off between statistics and position accuracy driven by the energy regime. 4FGL DR3 has a higher number of photons (because of the energy interval and the number of years covered). Thus, its sources can pass the test of significance more rigorously than in the case of having less photons to analyze. However the spatial resolution is worse due to a wider PSF at lower energies and consequently it might have a bigger problem of source
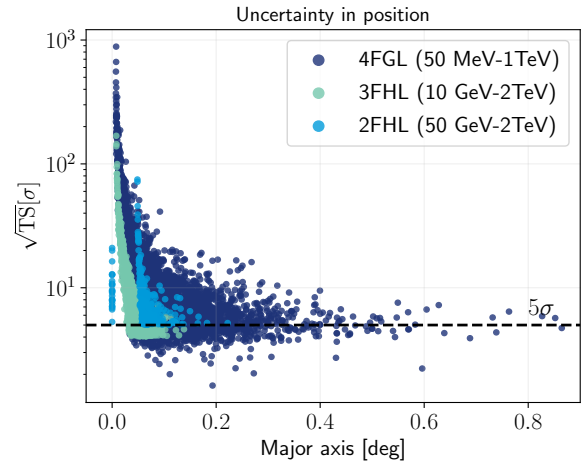
Fig. 11. Major axis of error ellipse at 95% confidence for the entire sample of 2FHL, 3FHL and 4FGL DR3 catalogs. Some of the scatter seen in 2FHL case arises from statistical effects.

confusion. The 3FHL/2FHL catalogs study the same number of years, and only differ in the energy range. The 3FHL catalog covers a larger energy range, and has higher statistics than 2FHL. The PSF in this case is also narrow, so its sources are in a very favorable position to rigorously pass significance tests and also reduce the problem of source confusion. Conversely, in the 2FHL catalog we see that the compromise between statistics and position resolution starts to brake. The high energies and low background levels make it possible for its sources to pass the significance tests with fewer photons but the determination of the position becomes more tricky and a greater dispersion is seen, even if the small value of the PSF does not allow the uncertainty to be very large.

Our catalog is in the middle of the 3FHL/2FHL catalogs[14], so we can assume that if the significance test is validly passed, the source confusion will not be a big problem to be concern about.

---

[14]Although we are almost doubling the years of data.
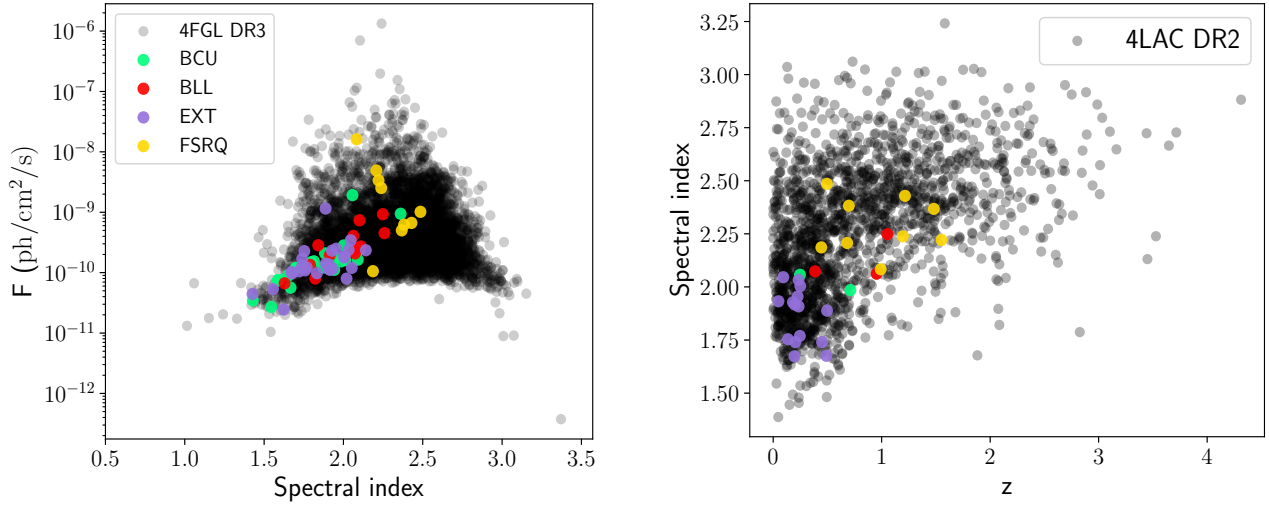
Fig. 12. (**Left**) Flux as a function of photon spectral index. (**Right**) Photon spectral index as a function of redshift. In this case we use the 4LAC DR2 catalog instead of the 4FGL DR3 as it contains the redshifts. For both graphs, we are using the spectral parameters included in the Fermi catalogs and not the ones derived in our study since the low number of photons considered in the analysis leads to high uncertainties in their determination.

4. Results and discussion

4.1. The catalog: A glimpse of the gamma-ray sky in the interval 30 GeV - 2 TeV.

Our algorithm provides us with a total of 2591 potential sources outside the Galactic plane ($|b| > 10°$). Of these, 850 were already identified in the 2FHL/3FHL catalogs, and hence discarded.

We are left with a total of 1741 seeds (329 with association in the 4FGL DR3) of which only the top 389 (124 in the 4FGL DR3) with higher fluxes were analysed. After the statistical significance study we end up with 90 potential candidates among which we had: BL Lacs (BLL), extreme BL Lacs (EXT), Flat Spectra Radio Quasars (FSRQ) and blazar candidates unclassified (BCU). The blazar type has been established primarily by looking at the type set by the 4FGL DR3 catalog and further improved from the SEDs coming from the SSDC page (21). Table 2 shows some of the parameters that characterise them.

Table 2. Compendium of the main features of this catalog

	$N_{sources}$	With z	γ	N_{pred}	TS
BLL	19	5	2.95	5.46	29.06
EXT	27	15	2.36	6.13	37.52
FSRQ	9	9	3.94	12.66	103.86
BCU/Unknown	34	2	3.06	5.78	31.36
New Sources	1	1	2.26	4.15	30.60
Total	90	32	2.91	6.51	40.07

Notes. $N_{sources}$ is the number of sources found of each type; the second column indicates the number of sources with determined redshift in the 4LAC DR2 catalog; γ is the mean photon spectral index; N_{pred} is the mean number of predicted photons; TS is the test statistic related with the σ-level detection.

- $N_{sources}$. There are a large number of BCU/Unknown type sources in our sample. This results from the need of a multi-wavelength coverage of the SED to proper determine the type, something difficult to obtain in many cases. We can see also that EXT are quite abundant while FSRQ are one of

the scarcest types in those energies.

- z. Redshift is a key factor when studying a source, especially in terms of detectability. However, determining the redshift for blazars is challenging since its intense brightness obscures the host galaxy, from which the redshift could be derived. We need emission or absorption lines in the optical spectrum to be observable and while this is possible for FSRQs, many BL Lacs have featureless optical spectra. For EXT we can see sometimes some hints of thermal emission from the host galaxy and/or torus making their redshift determination easier than for BLLs. Lastly, even if we have a large number of detected gamma-ray sources, a great number do not have multi-wavelength data to be analyzed. This is the case of BCUs for which redshift and type determination are not straightforward.

- γ. The spectral index reveals not only that the processes that dominate our sources are non-thermal but also whether they are hard sources (possibly extending at higher energies, small γ) or soft ones (staying at smaller energies, high γ). In Figure 12, we see that FSRQs are the softer ones. On one hand, their SED peaks are shifted to lower frequencies/energies and on the other, this type of blazar are usually located at higher redshifts having a higher absorption by EBL in the HE spectra part[15]. In contrast, they exhibit the highest fluxes as a consequence of the high accretion rates. FSRQs are followed by BCU/Unknown, BLL and EXT. This last one seems to be the hardest, picking at higher energies but with the lowest fluxes.

- N_{pred} and TS. The number of predicted photons for a source is not very high in this regime, as explained in the previous

---

[15]There are several factors that may contribute to these sources being less common at low redshifts. One of them is that lower redshifts cause the spectrum to move to higher energies where *Fermi*-LAT is less sensitive. Others can be the evolution of the Universe or the evolution of luminosity which decreases with time which makes low-redshift quasars harder to detect.
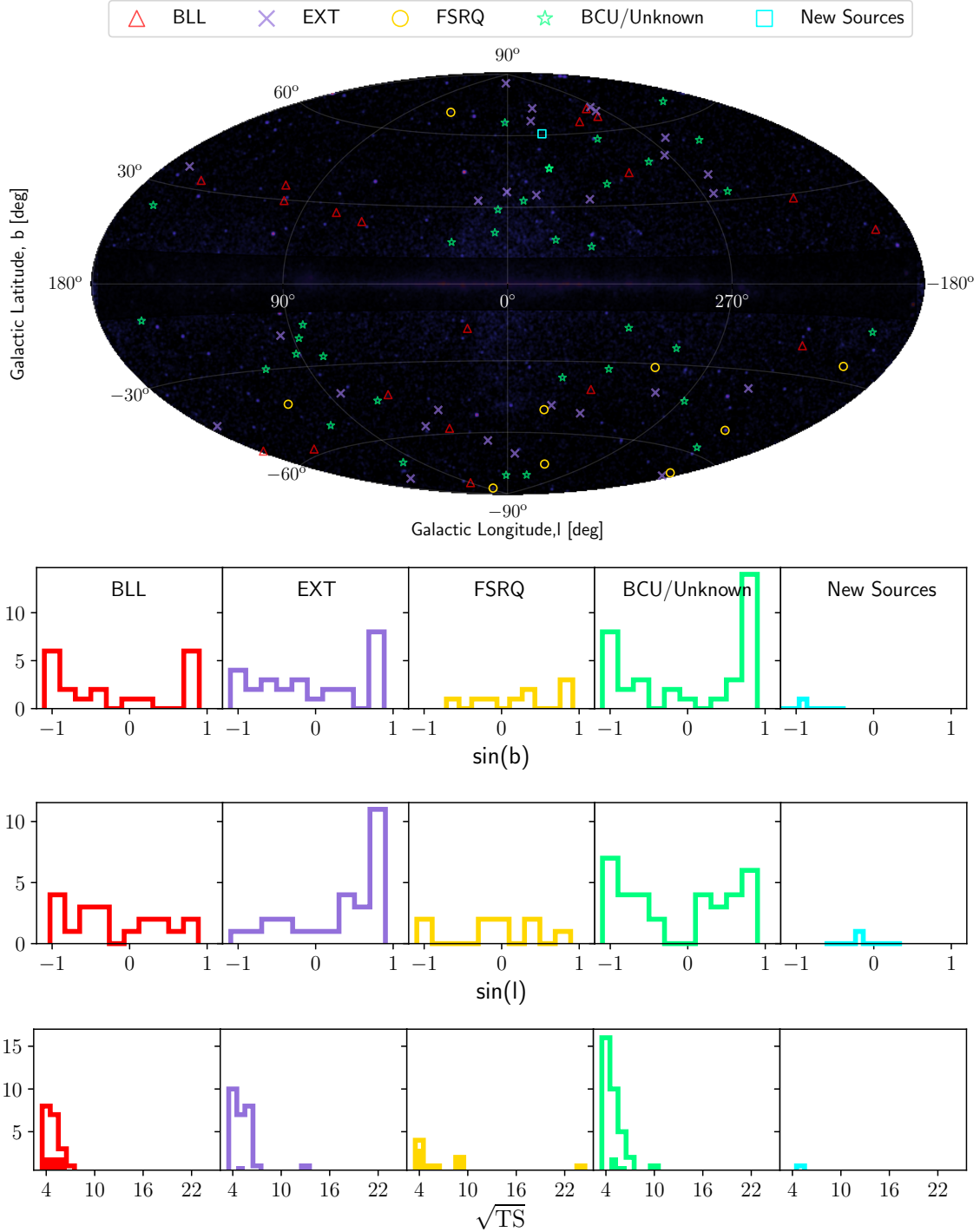
Fig. 13. (**Top**) Sky map of the sources found in this catalog according to their type. The galactic plane is not shown as it has not been considered in this work. (**Bottom**) Histograms comparing the position (latitude, b, and longitude, l) and $\sqrt{TS}$ for the different types of sources found. In this last graph, the coloured filled bars represent the number of variable sources.

section, and it is directly correlated with TS [16]. More photons implies a more robust detection and therefore a higher TS. On the other hand, fewer photons but with higher energies will also yield higher TS since they are less likely to be noise. Thus, the value of TS is affected by the combi-

nation of both the number of photons and their associated energy. Here we see that FSRQs shows the highest values of TS since their high luminosity, make them more detectable in case they manage to accelerate photons to the energy ranges considered. FSRQ are followed by the EXT and not far behind by BLL.

In Figure 13 we can see the spatial distribution of our sources in the *Fermi*-LAT skymap. For all types of blazars we

---

[16]If we recall the condition to consider an excess flux as a detection was to have a $TS > 16$ and $N_{pred} > 2$ for the case of sources with associations in the 4FGL DR3 and $TS > 25$ and $N_{pred} > 3$ for those without.
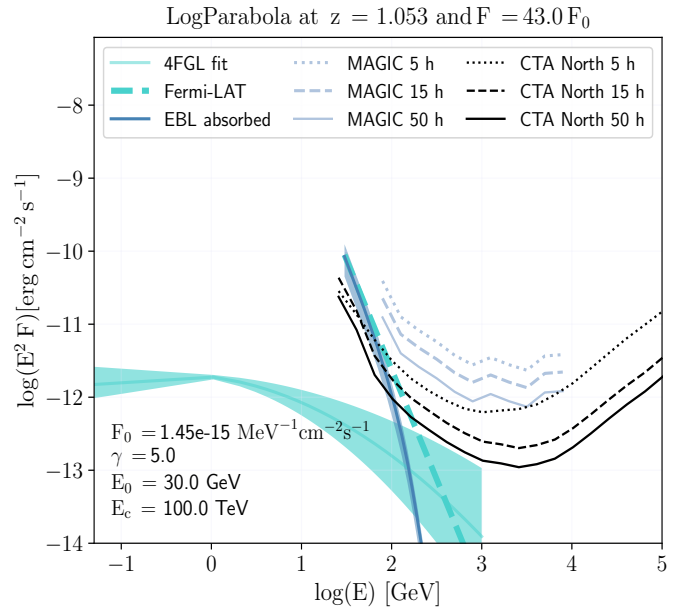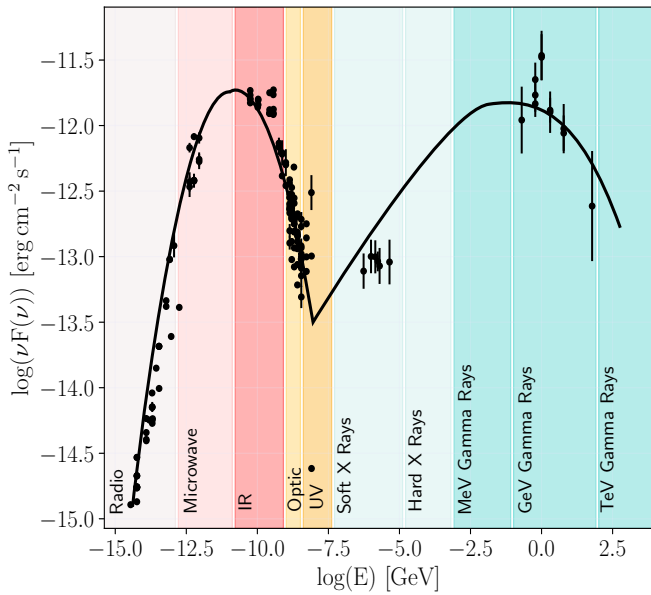
Fig. 14. (**Left**) SSDC SED of PMN J2206-0031 associated with J2206.8-0032 (BLL). Solid line connects dots with a mere visual purpose. (**Right**) Extrapolation of the SED to the regime where CTA/MAGIC are sensitive. The image header includes the spectrum fitting model, the source redshift and the factor that the flux needs to reach in order to be detected.

can see a roughly uniform distribution [17].

Regarding the TS, FSRQs and EXTs cover the widest range of values. This is due to the variability of some of the sources within these two types (shown as colloured filled bars in the $\sqrt{TS}$ histogram).

The description of the catalog and the tables including the spectral and detectability results are given at the end of this section. For some sources, the spectral parameters have high uncertainty values as a consequence of the low number of photons we are working with. However, it should be noted that our main interest here is to determine their TS, in order to establish a list of potential VHE candidates. The spectral parameters can be further refined when followed up by ground based telescopes if possible. Concerning the detectability, we have made an extrapolation of the Fermi SED to the energy regime of CTA/MAGIC, taking into account the Dominguez EBL model (32) for the absorption of the HE spectra. For this a redshift needs to be provided. Thus, sources without redshift are evaluated for three different cases z= 0.3, 0.5 and 1.

4.2. BL Lacs

Figure 14 shows how BLL have no sign of thermal emission. For them, the accretion regime is not radiatively efficient and can-not photo–ionize the BLR to sustain broad lines of luminosities comparable to the ones of FSRQs. The lack of external photons to be scattered at high frequencies implies less gamma ray emission (i.e. less Compton dominance), less radiative cooling and a larger average electron energy, resulting in a bluer spectrum. The case shown in Figure 14 would correspond to a low-frequency BLL.

---

[17]The negative values in sin(b) correspond to the upper part of the skymap and in sin(l) to the right part.
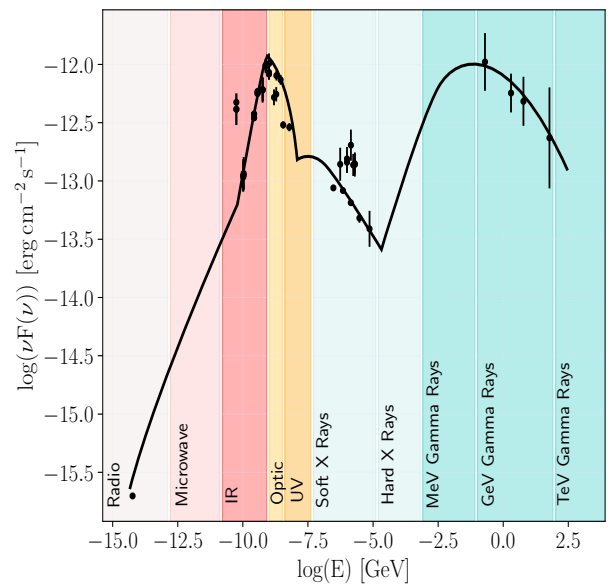
Fig. 15. SSDC SED of NVSS J104108-120332 associated with J1041.1-1201 (EXT). Solid line connects dots with a mere visual purpose.

For BLL we have 3 sources that can be detected by CTA within 5 h: J1637.7+7326, J0135.1+0255 and J0033.3-2040. The first two have no measured redshift but can still be detected up to z=1, although they would need 50 h with MAGIC due to its lower sensitivity. We could also detect J0723.7+2050 in case its redshift is z≤0.3.

If we increase the observation time to 15 h for CTA then we will be able to observe J2232.6-2023 and J0607.2-2518, both with known redshift, and J2211.4-7040 for z≤0.3.

For 50 h we could include J1807.9+4650 (up to redshift 0.3); J1925.8-2220, J1808.2+3500 and J2211.4-7040 (the three
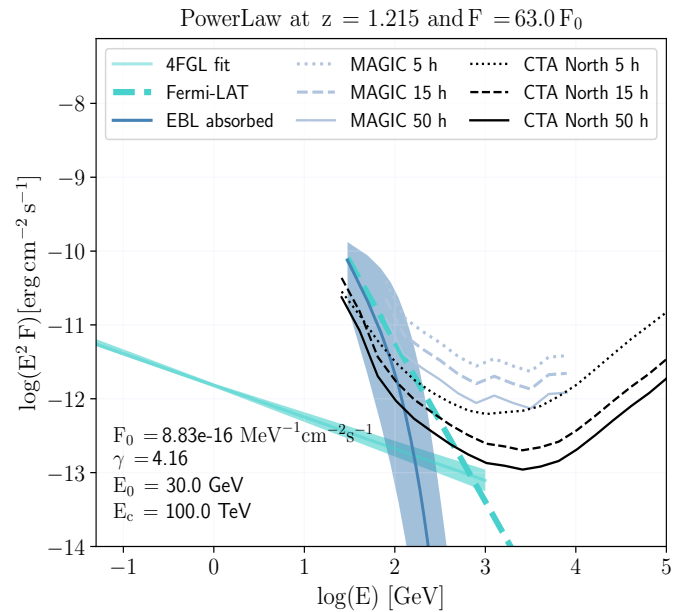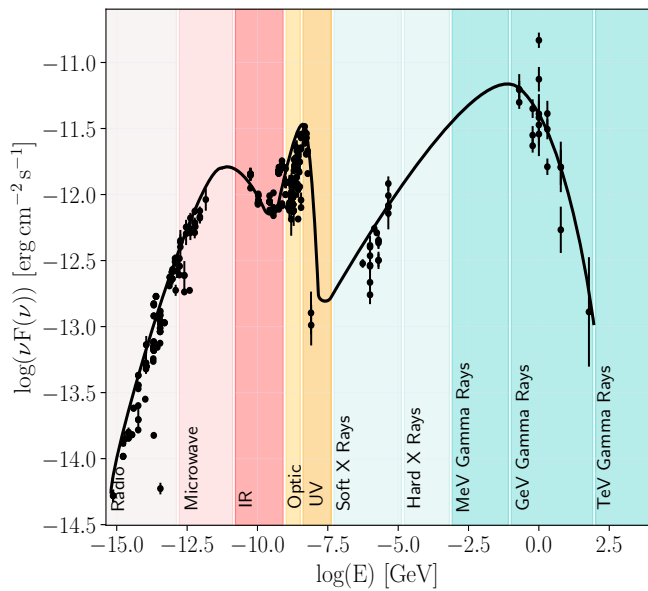
Fig. 16. (**Left**) SSDC SED of PKS 2204-54 associated with J2207.5-5346 (FSRQ). Solid line connects dots with a mere visual purpose. (**Right**) Extrapolation of the SED to the regime where CTA/MAGIC are sensitive. The image header includes the spectrum fitting model, the source redshift and the factor that the flux needs to reach in order to be detected.

up to z=0.5); J0859.2+0047 (up to z=1).

Other sources that are not detected in principle as J1238.3-1959, J0245.1-0257, J2206.8-0032 and J1800.1+7037 are variable sources so a further study would be needed to estimate whether they could reach the required fluxes and be considered as potential targets.

4.3. Extreme BL Lacs

Extreme blazars come in two flavors: extreme synchrotron (synchrotron peak beyond 1 keV) and extreme TeV sources (γ-ray peak energy above 1 TeV), a maximum where survey-mode instruments such as *Fermi*-LAT are often not sensitive enough. For the known extreme TeV blazars, the luminosity measured barely exceeds the *Fermi*-LAT sensitivity limit. This might suggest that the extremes identified so far are only the tip of the (faint) iceberg of the extreme TeV blazar population.

The faint luminosities together with the shift in wavelength of the peaks make the host galaxy sometimes visible in the spectrum (Figure 15), which facilitates the determination of the redshift for this type of sources. In our sample 15 out of 27 have a measured redshift.

Regarding the detectability, we have 9 EXT that can be detected by CTA in 5 h either with their real redshift or up to z=1 in case they do not have a measured value. This 9 sources are: J1544.3-0649, J1348.9+0756, J0830.0+5231, J1215.1+0731, J1310.6+2449, J2321.0-6308, J2201.9-1706, J0303.3+0555 and J2202.7-5637. Of these J1544.3-0649, J2321.0-6308, J2201.9-1706 and J2202.7-5637 could also be detected by MAGIC in 5 h. We can extend the list of CTA candidates within 5 h if J2331.2-3839, J0331.8-7040, J1407.5-2706 are located at z≤0.5 and if J2240.3-1246, J1516.4-1523 are at a z≤0.3.

If we increase the time of observation to 15 h with CTA we can include J2251.7-3208[18] and in 50 h: J1117.2+0008, J0110.7-1254, J1216.1+0930, J0505.8-3817, J2236.6+3706, J1041.1-1201 and J1131.1-0944 (the latter two only up to z=0.5).

4.4. FSRQ

As we have seen, FSRQs have high accretion rates and obscuring torus of dust that surrounds the accretion disc. All this translates into a more articulated SED where the typical double-peaked bumps are paired with several superimposed contributions (for example, Figure 16 where we can see the accretion disk).

The inverse Compton luminosity is large in FSRQs, due to the presence of external seed photons coming from the BLR and the torus that can re-isotropize part of the disc radiation. However, since the cooling rate is more severe (prompt Comptonization of low energy electrons with ambient photons), electrons attain smaller typical energies, explaining the redder spectrum.

FSRQs were not expected to emit VHE gamma rays due to their intrinsic morphology and steep HE gamma-ray spectra. However 8 FSRQs have been detected recently in the VHE band (mostly during flaring states), challenging the theoretical emission scenarios. Expanding the VHE FSRQ family is crucial to understand their physical properties and set constraints on the AGN structure and specifically on how VHE photons are absorbed when interacting with the different photon fields.

For FSRQs we have two possible targets to be detected by CTA in 5 h: J0348.6-2749 and J1422.5+3223, which corresponds with PKS 0346-27 and OQ334 (or B2 1420+32) respectively and have been included recently in the TeVCat catalog (33). Both of them can also be detected by MAGIC in 5

---

[18]Reported in Mireia et al (2021) (2).
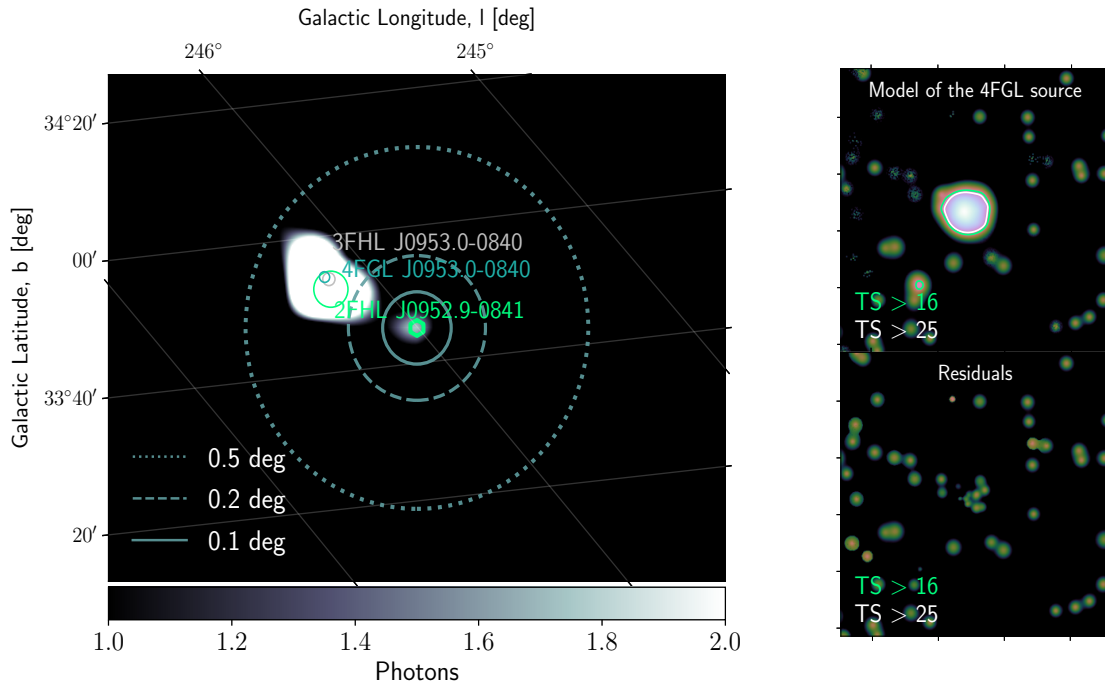
Fig. 17. (**Left**) Position of a candidate of 'New Source' in the skymap near to a catalogued one. (**Right**) TS map. In this case the model only includes the catalogued source. No traces of a new possible source is seen.
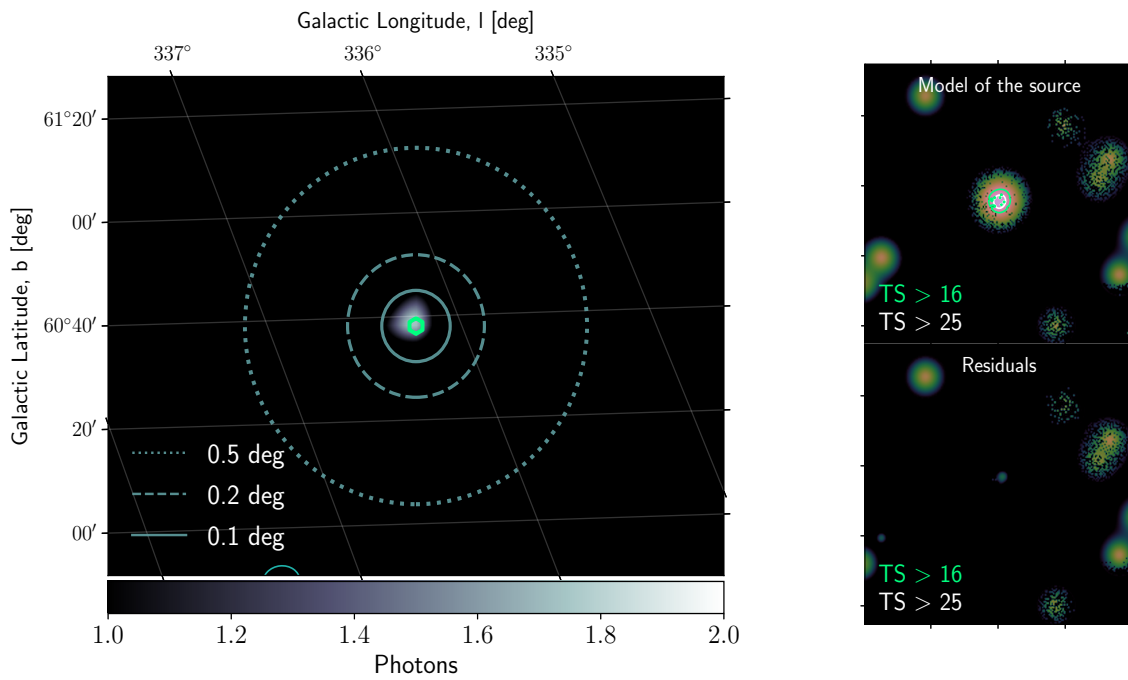
Fig. 18. (**Left**) Position of the 'New Source' in the skymap with no 4FGL DR3 association. (**Right**) TS map. We need to add a new source in order to fit the photon cluster. No residuals are left.

h.

For 15 h with CTA we can include in our list J0038.2-2459 and for 50 h J0028.5+2001. The rest of the sample do not reach the necessary fluxes required for a detection even though

they present large variability values so a further study would be needed for them.
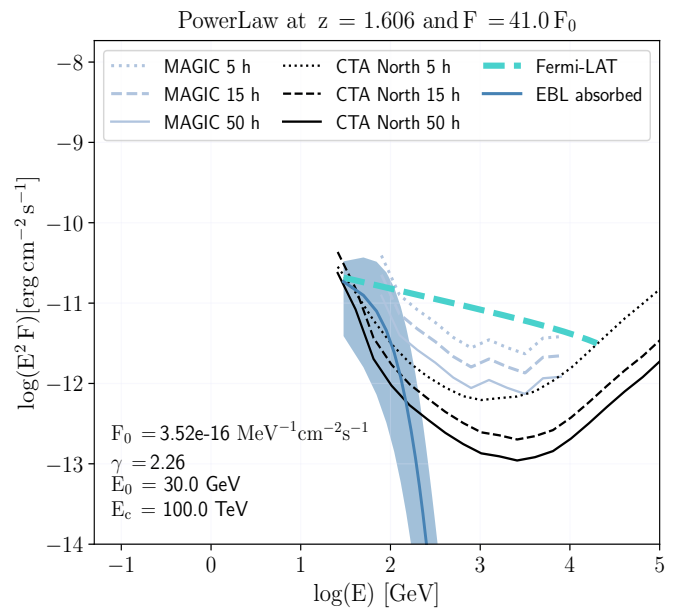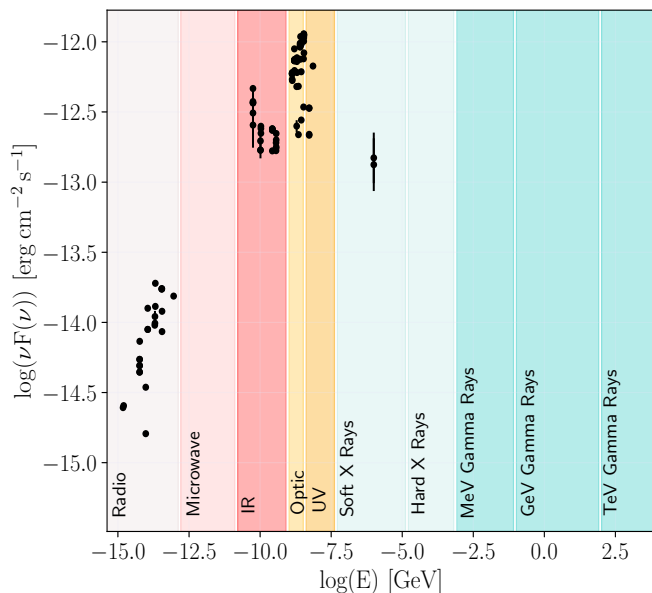
Fig. 19. (**Left**) SSDC SED of PKS 1351+021 ('New Source'). Solid line connects dots with a mere visual purpose. (**Right**) Extrapolation of the SED to the regime where CTA/MAGIC are sensitive. The image header includes the spectrum fitting model, the source redshift and the factor that the flux needs to reach in order to be detected.

4.5. BCU/Unknown

We only have 4 BCU/Unknown type sources that can be detected by CTA in 5 h either with their real redshift or up to z=1 in case they do not have a measured value. They are: J1416.1+1320 (which can also be detected by MAGIC in 5h), J2226.6+0210, J2207.1+2222 and J1646.7-1330. We can extend our target selection if the following sources are located at a z≤0.5: J1457.3-4246, J2210.8+3203, J1537.9-1344, J0011.8-3142, J1514.4-7719, J0733.3-7615. And if they are at z≤0.3, we will add J1158.8-1430, J0415.2-5741 and J1017.2-1549.

In 15 h with CTA we could detect also until z=1 J1614.8-0850; until z=0.5: J0013.4+0950, J2143.9+3337, J2241.3+2943, J0030.9-3618; and until z=0.3, J0315.4-2643.

Finally, for 50 h with CTA we could add J2057.6-7829 for z≤0.5 and J1039.6+0535, J0355.3+3909 for z≤0.3.

4.6. New Source

Among the initial 12 possible candidates for 'New Sources' (sources that may be detected at other wavelengths but not in the HE regime with *Fermi*-LAT), there were some artefacts such as the one shown in Figure 17, where we considered as a possible seed a photon clump close to a catalogued source with which it fail to meet the 0.2° spatial association criteria. All these cases were removed from our catalog after the TS map verification.

Only one case, which was not surrounded by other catalogued sources, successfully passed the TS map (Figure 18). However, this is indeed an unusual case as it does not appear in either the high or the low-energy Fermi catalogs. The fact that it does not appear in the high-energy catalogs could be explained, as in the rest of the cases, by the very low values of fluxes or because it may have emitted the HE photons in the years not analysed by the 2FHL/3FHL catalogs. However, if there is a trace at high energies when considering the 13 years, it would

be expected that this source would also accelerate photons at lower energies in this period, which seems not to be the case, or at least not with enough significance to have been included in the 4FGL DR3 catalog.

After evaluating its position and cross-matching with other near sources through the SSDC tool, we could see that it is at a distance of 0.024° from the FSRQ PKS 1351+021 (Figure 19). This possibly associated source has a redshift of 1.608 and would require a factor of approximately 41 to be detected by CTA in 5 hours.

However, the non-detection of Fermi in the low energy range does not seem to agree with the nature and spectrum of a FSRQ. One could rather think of an EXT but it does not seem to be any trace of these in the field. A deeper analysis of this region would be needed, extending our study to lower energies. However this remains beyond the scope of this work.

Column	Unit	Description
id		Identifier number in the initial list of 2591 seeds sorted from highest to lowest flux
Source		Source name in 4FGL DR3 if there is association or in this catalog 'Source_id'
ASSOC		Name of identified or likely associated source
ASSOC_TEV		Name of likely corresponding TeV source from TeVCat, if any
CLASS		Class designation for associated source
Redshift		Redshift in 4LAC DR2
Signif_Avg		Source significance in σ units over the 100 MeV to 1 TeV band
TS		TS value encounter in the significance test study
f0	$MeV^{-1}\,cm^{-2}\,s^{-1}$	Normalization flux at pivot energy E_b in Power Law fit ???
f0_error	$MeV^{-1}\,cm^{-2}\,s^{-1}$	Error on f0
Eb	MeV	Energy at which error on differential flux is minimal
index		Spectral index at pivot energy E_b when fitting with Power Law
index_error		Error on index
flux	$ph\,cm^{-2}\,s^{-1}$	Integral phton flux from 30 GeV to 2 TeV
flux_error	$ph\,cm^{-2}\,s^{-1}$	Error on flux
Npred		Predicted number of events in the model of a source
Value		Normalized flux in our sky map. The scale factor is $4.375 \cdot 10^{1}1$
Bin_30_2tev	ph	Counts in the interval 30 GeV to 2 TeV in the sky map
Bin1	ph	Counts in the interval 30 GeV to 69.4 GeV in the sky map
Bin2	ph	Counts in the interval 69.4 GeV to 109 GeV in the sky map
Bin3	ph	Counts in the interval 109 GeV to 149 GeV in the sky map
Bin4	ph	Counts in the interval 149 GeV to 189 GeV in the sky map
Bin5	ph	Counts in the interval 189 GeV to 2 TeV in the sky map
ra	deg	Right ascension encountered by the algorithm
dec	deg	Declination encountered by the algorithm
RAJ2000	deg	Right ascension of the 4FGL DR3 associated source
DEJ2000	deg	Declination of the 4FGL DR3 associated source
Conf_95_SemiMajor	deg	Long radius of error ellipse at 95% confidence for RAJ2000
Conf_95_SemiMinor	deg	Short radius of error ellipse at 95% confidence for DEJ2000
RA_Counterpart	deg	Right ascension of the counterpart ASSOC
DEC_Counterpart	deg	Declination of the counterpart ASSOC
Unc_Counterpart	deg	95% precision of the counterpart localization
SpectrumType		Spectrum type in the 4FGL DR3 (Power Law, Log Parabola)
Flux1000	$photons/cm^2/s$	The integral photon flux in 4FGL DR3 for 1-100 GeV
Pivot_Energy	MeV	Energy at which error on differential flux in 4FGL DR3 is minimal
LP_Index		Spectral index in 4FGL DR3 at pivot energy E_b when fitting with Log Parabola
Unc_LP_Index		Error on LP_Index
LP_beta		Curvature parameter in 4FGL DR3 (β in equation 6) when fitting with Log Parabola
Unc_LP_beta		Error on LP_beta
PL_Index		Spectral index in 4FGL DR3 at pivot energy E_b when fitting with Power Law
Unc_PL_Index		Error on PL_Index
Variability_Index		In 4FGL DR3, the sum of 2×log(Likelihood) difference between the flux fitted in each time interval and the average flux over the full catalog interval; a value greater than 24.72 over 12 intervals indicates <1% chance of being a steady source
CTA 5 03		F/F_{0t} to be detected by CTA in a 5 h exposure for a source at z=0.3
CTA 5 05		" at z=0.5
CTA 5 1		" at z=1
CTA 5 z		" at real z, if it is measured
CTA 15 03		F/F_0 to be detected by CTA in a 15 h exposure for a source at z=0.3
CTA 15 05		" at z=0.5
CTA 15 1		" at z=1
CTA 15 z		" at real z, if it is measured
CTA 50 03		F/F_0 to be detected by CTA in a 50 h exposure for a source at z=0.3
CTA 50 05		" at z=0.5
CTA 50 1		" at z=1
CTA 50 z		" at real z, if it is measured
MAGIC 5 03		F/F_0 to be detected by MAGIC in a 5 h exposure for a source at z=0.3
MAGIC 5 05		" at z=0.5
MAGIC 5 1		" at z=1
MAGIC 5 z		" at real z, if it is measured
MAGIC 15 03		F/F_0 to be detected by MAGIC in a 15 h exposure for a source at z=0.3
MAGIC 15 05		" at z=0.5
MAGIC 15 1		" at z=1
MAGIC 15 z		" at real z, if it is measured
MAGIC 50 03		F/F_0 to be detected by MAGIC in a 50 h exposure for a source at z=0.3
MAGIC 50 05		" at z=0.5
MAGIC 50 1		" at z=1
MAGIC 50 z		" at real z, if it is measured
Fmax estimation		Estimaton of the maximum flux of a source using Flux_History data max(Flux_History)/mean(Flux_History<mean(Flux_History))
Flux_History	$cm^{-2}\,s^{-1}$	In 4FGL DR3 integral photon flux from 100 MeV to 100 GeV in each year
Unc_Flux_History	$cm^{-2}\,s^{-1}$	In 4FGL DR3 1σ lower and upper error on integral photon flux in each year

Notes. The catalog can be found in
https://drive.google.com/file/d/1Lj17WCzBDuC5mQdFgd0jISjEpYqDDTMC/view?usp=sharing

Table 3. BLL Positions and Emission Properties

| | | | Position | | | Emission properties | | | | | | | | | | | | | | |
| | | | | | | TS anaysis results | | | | | | | Flux map | Count map | | | | | | Var |
Source in 4FGL	ASSOC	TS	Ra [deg]	Dec [deg]	ΔD[deg]	F_0	$u(F_0)$	γ	$u(\gamma)$	F	u(F)	N_{pred}	Value	Total	Bin1	Bin2	Bin3	Bin4	Bin5	
J0723.7+2050	GB6 J0723+2051	50.15	110.95	20.84	0.054	5.44E-16	2.95E-16	1.84	0.43	1.82E-11	6.19E-12	10.03	2.48	3	2	0	1	0	0	15.22
J1807.9+4650	RGB J1808+468	48.52	272.00	46.84	0.064	6.16E-16	3.44E-16	2.76	0.74	1.05E-11	4.09E-12	7.01	2.08	3	3	0	0	0	0	12.64
J1238.3-1959	PMN J1238-1959	44.01	189.59	-19.99	0.028	1.36E-15	7.66E-16	3.86	1.08	1.43E-11	5.58E-12	7.61	3.47	4	4	0	0	0	0	39.54
J1637.7+7326	RX J1637.9+7326	36.32	249.45	73.44	0.087	3.83E-16	2.46E-16	2.39	0.71	8.09E-12	3.47E-12	6.05	2.48	4	2	2	0	0	0	28.90
J0245.1-0257		34.65	41.29	-2.96	0.096	1.55E-15	6.54E-16	5.00	0.27	1.16E-11	4.85E-12	6.15	1.74	2	2	0	0	0	0	48.75
J1219.7+0444	NVSS J121945+044621	31.95	184.94	4.75	0.093	1.32E-15	6.41E-16	5.00	0.00	9.93E-12	4.80E-12	5.22	1.75	2	2	0	0	0	0	15.36
J1925.8-2220	TXS 1922-224	29.70	291.47	-22.34	0.084	6.60E-16	4.24E-16	2.53	0.70	1.28E-11	5.52E-12	7.02	2.51	3	1	2	0	0	0	8.58
J0812.8+6507	GB6 J0812+6508	27.88	123.22	65.13	0.025	4.75E-16	3.07E-16	2.69	0.83	8.36E-12	3.81E-12	5.68	2.04	3	3	0	0	0	0	18.78
J1808.2+3500	MG2 J180813+3501	26.50	272.07	35.01	0.030	2.59E-16	1.84E-16	2.00	0.59	7.56E-12	3.62E-12	4.91	2.13	3	1	2	0	0	0	41.34
J0135.1+0255	1RXS J013506.7+025558	25.77	23.78	2.92	0.091	4.30E-16	3.61E-16	2.25	1.11	9.38E-12	4.64E-12	4.93	1.75	2	1	1	0	0	0	23.32
J2232.6-2023	NVSS J223248-202226	25.68	338.17	-20.39	0.024	3.03E-16	2.54E-16	1.94	0.77	8.80E-12	4.44E-12	4.55	1.78	2	0	2	0	0	0	15.73
J0033.3-2040	RBS 0075	23.85	8.35	-20.67	0.054	1.89E-16	1.70E-16	1.74	0.74	6.68E-12	3.78E-12	3.50	1.75	2	2	0	0	0	0	7.81
J0607.2-2518	1RXS J060714.2-251855	23.85	91.82	-25.31	0.024	1.56E-16	1.47E-16	1.62	0.80	6.00E-12	3.41E-12	3.41	2.43	3	2	0	1	0	0	14.33
J2206.8-0032	PMN J2206-0031	23.08	331.71	-0.55	0.084	1.45E-15	6.82E-16	5.00	0.01	1.08E-11	5.09E-12	5.63	1.77	2	2	0	0	0	0	107.85
J1250.6+0217	PKS 1247+025	22.46	192.65	2.29	0.137	8.00E-16	5.00E-16	3.07	1.25	1.44E-06	1.01E-05	5.72	1.75	2	2	0	0	0	0	14.17
J1800.1+7037	RX J1759.8+7037	20.01	270.03	70.63	0.044	6.00E-16	5.00E-16	4.20	1.73	4.92E-04	4.81E-03	4.37	1.88	3	3	0	0	0	0	29.26
J0859.2+0047	RGB J0859+007	19.98	134.82	0.79	0.091	6.21E-16	4.91E-16	3.36	1.24	7.90E-12	4.30E-12	4.16	1.75	2	2	0	0	0	0	10.81
J1223.5+0818	SDSS J122327.49+082030.4	19.43	185.88	8.30	0.066	6.01E-16	4.27E-16	3.15	1.08	8.38E-12	4.34E-12	4.47	1.73	2	2	0	0	0	0	23.54
J2211.4-7040	PMN J2211-7039	18.34	332.86	-70.68	0.255	1.69E-16	1.63E-16	1.63	0.82	6.38E-12	3.72E-12	3.38	1.74	2	1	0	1	0	0	17.82

Notes. (**Position section**) Ra and Dec are the positions of the associated 4FGL source and ΔD the difference in distance between the position we have identified with the algorithm and the catalogued one. (**Emission properties section**) F_0 is the normalization flux ($MeV^{-1} cm^{-2} s^{-1}$); γ the spectral index; F the integrated photon flux from 30 GeV to 2 TeV ($ph\,cm^{-2}\,s^{-1}$) and N_{pred} the number of predicted photons in the model. Flux map and count map values are the normalized flux (x $4.375 10^{11}\ ph\,cm^{-2}\,s^{-1}$) and the number of photons encounter in a specific position in our sky map. Bin1 goes from 30 GeV to 69 GeV; Bin2 from 69 GeV to 109 GeV: Bin3 from 109 GeV to 149 GeV: Bin4 from 149 GeV to 189 GeV and Bin5 from 189 GeV to 2 TeV. The pivot energy, E_b was fixed to 30 GeV. Finally we consider a source is variable if $Var > 24.72$.

Table 4. BLL Detectability

Source in 4FGL	ASSOC	z	CTA									MAGIC									$F_{max,est}$
			5 h			15 h			50 h			5 h			15 h			50 h			
			$z_{0.3}$	$z_{0.5}^*$	z_1	$z_{0.3}$	$z_{0.5}^*$	z_1	$z_{0.3}$	$z_{0.5}^*$	z_1	$z_{0.3}$	$z_{0.5}^*$	z_1	$z_{0.3}$	$z_{0.5}^*$	z_1	$z_{0.3}$	$z_{0.5}^*$	z_1	
J0723.7+2050	GB6 J0723+2051	-	2.7	4.3	9.9	1.4	2.3	5.5	0.8	1.3	3.0	15.6	23.7	55.2	9.0	13.7	31.9	4.9	7.5	17.5	3.9
J1807.9+4650	RGB J1808+468	-	13.2	15.7	24.0	7.1	8.7	14.5	3.9	4.8	8.0	65.9	81.0	154.2	38.0	46.8	89.0	20.8	25.6	48.8	4.1
J1238.3-1959	PMN J1238-1959	-	20.4	21.6	27.6	12.3	13.1	16.8	6.8	7.2	9.2	130.8	138.5	177.8	75.5	80.0	102.7	41.4	43.8	56.2	3.0
J1637.7+7326	RX J1637.9+7326	-	11.3	15.7	28.4	6.1	8.7	16.2	3.4	4.8	8.9	62.3	76.6	178.1	35.9	44.2	102.8	19.7	24.2	56.3	29.6
J0245.1-0257		-	36.9	37.9	43.2	28.3	30.0	38.5	15.5	16.4	21.1	300.2	318.0	408.2	173.3	183.6	235.7	94.9	100.5	129.1	5.7
J1219.7+0444	NVSS J121945+044621	-	43.4	44.6	50.9	33.3	35.3	45.3	18.3	19.3	24.8	353.7	374.6	480.9	204.2	216.3	277.7	111.9	118.4	152.1	3.5
J1925.8-2220	TXS 1922-224	-	8.3	10.9	18.5	4.5	6.0	11.2	2.5	3.3	6.1	44.1	54.2	118.7	25.4	31.3	68.5	13.9	17.1	37.5	4.2
J0812.8+6507	GB6 J0812+6508	-	15.2	18.6	29.5	8.2	10.3	17.8	4.5	5.7	9.8	77.4	95.2	188.9	44.7	55.0	109.1	24.5	30.1	59.7	3.1
J1808.2+3500	MG2 J180813+3501	-	8.0	12.0	25.8	4.3	6.5	14.4	2.40	3.6	7.9	45.1	63.4	147.5	26.0	36.6	85.2	14.3	20.1	46.7	3.9
J0135.1+0255	1RXS J013506.7+025558	-	7.8	11.2	21.5	4.2	6.1	12.0	2.3	3.3	6.6	44.2	55.2	128.3	25.5	31.8	74.1	14.0	17.4	40.6	44.5
J2232.6-2023	NVSS J223248-202226	0.386		7.5			4.1			2.2			42.6			24.6			13.5		4.4
J0033.3-2040	RBS 0075	0.073		2.5			1.0			0.5			10.7			6.2			3.4		6.0
J0607.2-2518	1RXS J060714.2-251855	0.275		5.6			3.0			1.6			31.8			18.3			10.0		4.8
J2206.8-0032	PMN J2206-0031	1.053		47.2			42.6			23.3			451.4			260.6			142.7		4.0
J1250.6+0217	PKS 1247+025	0.954		23.5			14.2			7.8			151.0			87.2			47.7		2.4
J1800.1+7037	RX J1759.8+7037	-	61.6	65.2	74.4	37.3	39.4	50.6	20.4	21.6	27.7	395.2	418.5	537.3	228.1	241.6	310.2	125.0	132.3	169.9	4.5
J0859.2+0047	RGB J0859+007	-	29.2	31.0	39.8	16.3	18.7	24.0	9.0	10.3	13.2	158.3	194.7	255.0	91.4	112.4	147.2	50.1	61.6	80.6	12.3
J1223.5+0818	SDSS J122327.49+082030.4	-	23.2	26.9	34.5	12.9	14.9	20.8	7.1	8.2	11.4	120.8	148.5	221.2	69.7	85.8	127.7	38.2	47.0	69.9	6.1
J2211.4-7040	PMN J2211-7039	-	5.7	9.8	24.6	3.0	5.3	13.7	1.7	2.9	7.5	33.4	56.9	132.4	19.3	32.9	76.4	10.6	18.0	41.9	3.4

Notes. (**Position section**) Ra and Dec are the positions of the associated 4FGL source and ΔD the difference in distance between the position we have identified with the algorithm and the catalogued one. (**Emission properties section**) F_0 is the normalization flux ($MeV^{-1}cm^{-2}s^{-1}$); γ the spectral index; F the integrated photon flux from 30 GeV to 2 TeV ($ph\,cm^{-2}\,s^{-1}$) and N_{pred} the number of predicted photons in the model. Flux map and count map values are the normalized flux (x $4.375 10^{11}$ $ph\,cm^{-2}\,s^{-1}$) and the number of photons encounter in a specific position in our sky map. Bin1 goes from 30 GeV to 69 GeV; Bin2 from 69 GeV to 109 GeV: Bin3 from 109 GeV to 149 GeV: Bin4 from 149 GeV to 189 GeV and Bin5 from 189 GeV to 2 TeV. The pivot energy, E_b was fixed to 30 GeV. Finally we consider a source is variable if $Var > 24.72$.

Table 5. EXT Positions and Emission Properties

Source in 4FGL	ASSOC	TS	Ra [deg]	Dec [deg]	ΔD[deg]	F_0	$u(F_0)$	γ	$u(\gamma)$	F	u(F)	N_{pred}	Flux map Value	Total	Bin1	Bin2	Bin3	Bin4	Bin5	Var
J1544.3-0649	NVSS J154419-064913	194.89	236.08	-6.83	0.013	1.91E-15	5.98E-16	1.99	0.30	5.34E-11	1.05E-11	29.04	10.94	13	7	5	1	0	0	587.23
J1117.2+0008	RX J1117.2+0006	57.85	169.30	0.14	0.107	1.75E-15	8.80E-16	3.71	0.95	1.94E-11	6.61E-12	10.04	1.78	2	1	1	0	0	0	15.10
J1348.9+0756	1RXS J134853.8+075704	48.32	207.25	7.94	0.029	3.25E-16	2.58E-16	1.55	0.93	1.05E-11	4.61E-12	5.78	4.19	5	3	2	0	0	0	15.01
J0830.0+5231	RX J0830.1+5230	45.75	127.51	52.53	0.028	3.42E-16	2.19E-16	1.77	0.54	1.18E-11	4.58E-12	7.27	2.23	3	2	1	0	0	0	12.09
J0110.7-1254	1RXS J011050.0-125455	42.88	17.69	-12.91	0.046	6.59E-16	4.14E-16	2.62	0.75	1.21E-11	5.33E-12	6.34	2.64	3	2	1	0	0	0	12.39
J1328.6+1145	2E 1326.1+1200	41.75	202.17	11.76	0.078	1.13E-15	6.92E-16	3.98	1.29	1.14E-11	4.78E-12	6.29	2.50	3	3	0	0	0	0	11.90
J0215.2-1619	NVSS J021515-161738	41.14	33.80	-16.33	0.080	5.58E-16	3.96E-16	3.20	1.11	7.62E-12	3.81E-12	4.10	1.71	2	1	1	0	0	0	5.91
J1215.1+0731	1ES 1212+078	40.83	183.79	7.52	0.074	3.39E-16	2.20E-16	1.64	0.52	1.32E-11	5.25E-12	7.00	1.74	2	2	0	0	0	0	17.45
J1310.6+2449	CRATES J131038.52+244822.1	37.36	197.65	24.83	0.067	1.00E-16	1.00E-16	0.93	0.62	2.09E-11	3.64E-11	4.82	2.40	3	1	1	1	0	0	13.81
J1216.1+0930	TXS 1213+097	36.01	184.04	9.51	0.078	6.89E-16	4.12E-16	2.63	0.73	1.27E-11	5.29E-12	6.78	3.45	4	2	2	0	0	0	11.70
J2321.0-6308	2MASS J23203986-6309181	31.66	350.26	-63.14	0.110	6.37E-17	7.83E-17	0.50	0.88	7.17E-12	3.73E-12	3.85	1.72	2	0	2	0	0	0	9.22
J2251.7-3208	1RXS J225146.9-320614	31.59	342.94	-32.14	0.049	5.25E-16	3.42E-16	2.23	0.62	1.26E-11	5.47E-12	6.60	1.76	2	1	1	0	0	0	9.55
J2201.9-1706	RBS 1813	30.43	330.49	-17.11	0.046	1.33E-16	1.27E-16	1.24	0.71	7.55E-12	3.88E-12	3.91	2.66	3	1	1	1	0	0	8.66
J0505.8-3817	1RXS J050559.9-382059	28.74	76.47	-38.30	0.069	8.46E-16	5.33E-16	3.06	1.03	1.20E-11	4.92E-12	7.04	2.38	3	2	1	0	0	0	27.22
J2331.2-3839	NVSS J233123-384043	28.54	352.82	-38.66	0.037	2.65E-16	2.09E-16	1.87	0.72	8.55E-12	4.27E-12	4.53	2.61	3	2	1	0	0	0	16.43
J1037.0-1954	1RXS J103657.5-195432	28.20	159.27	-19.90	0.034	6.88E-16	5.16E-16	3.21	1.32	9.36E-12	4.49E-12	5.04	1.71	2	2	0	0	0	0	8.47
J0331.8-7040	SUMSS J033202-703952	26.74	52.97	-70.67	0.065	4.39E-16	3.14E-16	2.60	0.86	8.17E-12	4.13E-12	4.47	2.54	3	2	1	0	0	0	14.71
J1041.1-1201	NVSS J104108-120332	24.93	160.29	-12.03	0.053	2.53E-16	2.10E-16	2.11	0.79	6.69E-12	3.79E-12	3.51	2.63	3	2	1	0	0	0	14.42
J0303.3+0555	GB6 J0303+0554	24.50	45.85	5.92	0.038	2.94E-16	2.62E-16	1.68	1.07	8.79E-12	4.42E-12	4.69	1.72	2	2	0	0	0	0	9.50
J2240.3-1246	1RXS J224014.7-124736	23.95	340.09	-12.78	0.029	3.84E-16	2.75E-16	2.14	0.64	9.92E-12	4.67E-12	5.07	1.80	2	0	2	0	0	0	8.99
J1407.5-2706	ESO 140425-2655.2	23.63	211.89	-27.10	0.052	2.91E-16	2.22E-16	1.64	0.73	1.04E-11	4.64E-12	5.62	2.54	3	2	1	0	0	0	9.96
J2202.7-5637	MS 2159.5-5649	23.13	330.70	-56.63	0.040	1.90E-16	1.84E-16	1.59	0.84	7.42E-12	4.13E-12	3.98	1.71	2	2	0	0	0	0	7.84
J2236.6+3706	NVSS J223626+370713	22.05	339.16	37.10	0.028	3.73E-16	3.09E-16	3.09	1.22	5.34E-12	3.11E-12	3.24	2.29	3	3	0	0	0	0	19.50
J2252.6+1245	2MASS J22523220+1245109	20.88	343.17	12.75	0.037	1.10E-15	7.79E-16	4.59	1.84	9.22E-12	4.71E-12	5.03	2.54	3	3	0	0	0	0	13.19
J1131.1-0944	1RXS J113104.6-094353	20.00	172.79	-9.74	0.018	2.42E-16	2.17E-16	2.11	0.81	6.35E-12	3.70E-12	3.29	1.78	2	2	0	0	0	0	18.65
J1621.3-0030	NVSS J162115-003137	19.34	245.35	-0.51	0.071	8.75E-16	6.27E-16	4.05	1.76	8.62E-12	4.42E-12	4.81	2.48	3	3	0	0	0	0	13.12
J1516.4-1523	RBS 1478	17.89	229.11	-15.39	0.011	2.36E-16	2.23E-16	2.02	1.01	6.19E-12	3.64E-12	3.34	2.54	3	2	1	0	0	0	14.05

Notes. (**Position section**) Ra and Dec are the positions of the associated 4FGL source and ΔD the difference in distance between the position we have identified with the algorithm and the catalogued one. (**Emission properties section**) F_0 is the normalization flux ($MeV^{-1} cm^{-2} s^{-1}$); γ the spectral index; F the integrated photon flux from 30 GeV to 2 TeV ($ph\,cm^{-2}\,s^{-1}$) and N_{pred} the number of predicted photons in the model. Flux map and count map values are the normalized flux (x $4.375 10^{11}\ ph\,cm^{-2}\,s^{-1}$) and the number of photons encounter in a specific position in our sky map. Bin1 goes from 30 GeV to 69 GeV; Bin2 from 69 GeV to 109 GeV: Bin3 from 109 GeV to 149 GeV: Bin4 from 149 GeV to 189 GeV and Bin5 from 189 GeV to 2 TeV. The pivot energy, E_b was fixed to 30 GeV. Finally we consider a source is variable if $Var > 24.72$.

Table 6. EXT Detectability

			Detectability F/F_0																	
			CTA									MAGIC									
Source in 4FGL	ASSOC	z	5 h			15 h			50 h			5 h			15 h			50 h			$F_{max,est}$
			$z_{0.3}$	$z^*_{0.5}$	z_1	$z_{0.3}$	$z^*_{0.5}$	z_1	$z_{0.3}$	$z^*_{0.5}$	z_1	$z_{0.3}$	$z^*_{0.5}$	z_1	$z_{0.3}$	$z^*_{0.5}$	z_1	$z_{0.3}$	$z^*_{0.5}$	z_1	
J1544.3-0649	NVSSJ154419-064913	-	1.1	1.6	3.5	0.6	0.9	1.9	0.3	0.5	1.1	6	8.5	19.8	3.5	4.9	11.4	1.9	2.7	6.3	44.5
J1117.2+0008	RXJ1117.2+0006	0.451		14.6			8.8			4.8			93.5			54.0			29.6		4.5
J1348.9+0756	1RXSJ134853.8+075704	0.25		2.2			1.2			0.6			11.7			6.8			3.7		5.8
J0830.0+5231	RXJ0830.1+5230	0.205		2.9			1.5			0.8			15.5			9.0			4.9		7.1
J0110.7-1254	1RXSJ011050.0-125455	0.234		8.9			4.8			2.7			48.1			27.8			15.2		2.6
J1328.6+1145	2E1326.1+1200	0.490		28.7			17.4			9.5			184.3			106.4			58.3		4.7
J0215.2-1619	NVSSJ021515-161738	-	26.5	30.0	38.6	14.7	17.1	23.3	8.1	9.3	12.8	138.9	170.9	247.4	80.2	98.7	142.9	43.9	54.0	78.2	4.4
J1215.1+0731	1ES1212+078	0.136		1.6			0.8			0.4			7.6			4.40			2.40		4.1
J1310.6+2449	CRATESJ131038.52+244822.1	0.226		1.4			0.7			0.4			6.5			3.7			2.1		3.1
J1216.1+0930	TXS1213+097	0.094		7.0			3.7			2.0			40.5			23.4			12.8		2.6
J2321.0-6308	2MASSJ23203986-6309181	0.200		0.4			0.1			0.06			1.3			0.7			0.4		3.5
J2251.7-3208	1RXSJ225146.9-320614	0.246		5.5			2.9			1.6			31.0			17.9			9.8		4.0
J2201.9-1706	RBS1813	-	3.1	6.2	18.7	1.7	3.4	10.4	0.9	1.8	5.7	16.7	33.8	93.8	9.7	19.5	54.1	5.3	10.7	29.6	3872.3
J0505.8-3817	1RXSJ050559.9-382059	0.182		13.8			7.6			4.2			68.8			39.7			21.8		4.9
J2331.2-3839	NVSSJ233123-384043	-	6.0	9.5	21.5	3.2	5.1	11.9	1.8	2.8	6.5	34.5	51.6	119.9	19.9	29.8	69.3	10.9	16.3	37.9	16.9
J1037.0-1954	1RXSJ103657.5-195432	-	21.8	24.6	31.5	12.1	14.0	19.1	6.6	7.7	10.4	114.1	140.4	202.2	65.9	81.0	116.7	36.1	44.4	63.9	5.1
J0331.8-7040	SUMSSJ033202-703952	-	14.1	17.9	29.5	7.6	9.9	17.8	4.2	5.4	9.8	73.3	90.2	189.2	42.3	52.0	109.3	23.2	28.5	59.8	20.5
J1041.1-1201	NVSSJ104108-120332	-	10.3	14.9	30.4	5.5	8.0	16.9	3.0	4.4	9.3	56.9	76.0	176.9	32.8	43.9	102.1	18.0	24.0	55.9	3.1
J0303.3+0555	GB6J0303+0554	0.196		2.7			1.4			0.8			14.2			8.2			4.5		7.6
J2240.3-1246	1RXSJ224014.7-124736	-	7.3	10.4	21	3.9	5.6	11.7	2.2	3.1	6.4	40.2	52.8	122.8	23.2	30.5	70.9	12.7	16.7	38.8	8.6
J1407.5-2706	ESO140425-2655.2	-	3.4	5.8	14.5	1.8	3.1	8	1.0	1.7	4.4	19.8	33.4	77.7	11.4	19.3	44.9	6.2	10.6	24.6	7.7
J2202.7-5637	MS2159.5-5649	0.049		1.1			0.3			0.2			3.8			2.2			1.2		4.4
J2236.6+3706	NVSSJ223626+370713	0.235		33.3			18.5			10.1			168.7			97.4			53.4		13.1
J2252.6+1245	2MASSJ22523220+1245109	0.496		43.4			30.0			16.4			317.9			183.5			100.5		8.6
J1131.1-0944	1RXSJ113104.6-094353	-	10.9	15.6	32	5.8	8.5	17.8	3.2	4.6	9.7	59.9	79.9	185.9	34.6	46.2	107.3	18.9	25.3	58.8	5.0
J1621.3-0030	NVSSJ162115-003137	-	37.1	39.3	47.2	22.5	23.8	30.5	12.3	13.0	16.7	238.2	252.2	323.8	137.5	145.6	187	75.3	79.8	102.4	5.0
J1516.4-1523	RBS1478	-	9.2	13.7	29.1	4.9	7.4	16.2	2.7	4.1	8.9	51.5	71.7	166.8	29.7	41.4	96.3	16.3	22.7	52.8	11.5

Notes. Factor that the flux of a source has to reach, with respect to its quiescent state to be detected by CTA and MAGIC at different exposure times and for different redshifts. In case the redshift is measured we only show the value of the factor for that specific z in the column $z^*_{0.5}$, the remaining values in $z_{0.3}$ and z_1 are empty. $F_{max,est}$ is a rough estimation of the maximum flux reached by the source in the 12 years covered by 4FGL DR3. It is computed as max(Flux_History)/mean(Flux_History<mean(Flux_History)).

Table 7. FSRQ Positions and Emission Properties

| | | | Position | | | Emission Properties | | | | | | | Flux map | Count map | | | | | | |
Source in 4FGL	ASSOC	TS	Ra [deg]	Dec [deg]	$\Delta D[deg]$	F_0	$u(F_0)$	γ	$u(\gamma)$	F	u(F)	N_{pred}	Value	Total	Bin1	Bin2	Bin3	Bin4	Bin5	Var
J0348.6-2749	PKS 0346-27	600.36	57.15	-27.82	0.080	1.23E-14	2.20E-15	4.27	0.42	1.13E-10	1.43E-11	63.86	13.07	16	16	0	0	0	0	19059.18
J0038.2-2459	PKS 0035-252	94.02	9.56	-24.99	0.098	2.86E-15	8.74E-16	5.00	0.15	2.14E-11	6.52E-12	11.40	4.34	5	5	0	0	0	0	2709.92
J1422.5+3223	OQ 334	86.16	215.64	32.38	0.074	1.21E-15	4.89E-16	2.72	0.50	2.10E-11	6.14E-12	12.88	3.77	5	3	2	0	0	0	9817.71
J0028.5+2001	TXS 0025+197	46.58	7.13	20.02	0.063	1.91E-15	6.73E-16	5.00	0.04	1.43E-11	5.04E-12	7.98	2.47	3	3	0	0	0	0	5813.57
J0030.3-4224	PKS 0027-426	30.92	7.60	-42.41	0.037	4.42E-16	3.43E-16	2.70	1.19	7.43E-12	3.75E-12	4.06	2.54	3	2	1	0	0	0	138.98
J0222.0-1616	PKS 0219-164	21.83	35.52	-16.28	0.021	5.10E-16	3.70E-16	3.08	1.11	1.05E-06	6.63E-06	3.95	1.71	2	1	1	0	0	0	237.52
J2207.5-5346	PKS 2204-54	20.78	331.89	-53.77	0.122	8.83E-16	6.71E-16	4.16	1.69	8.35E-12	4.28E-12	4.49	2.57	3	3	0	0	0	0	94.28
J0505.8-0419	S3 0503-04	17.61	76.46	-4.32	0.025	6.01E-16	5.07E-16	4.15	1.91	5.73E-12	3.39E-12	3.06	1.72	2	2	0	0	0	0	65.31
J0449.6-8100	PKS 0454-81	16.46	72.40	-81.01	0.082	4.72E-16	4.68E-16	4.37	2.30	4.21E-12	2.98E-12	2.24	1.75	2	2	0	0	0	0	17.05

Notes. (**Position section**) Ra and Dec are the positions of the associated 4FGL source and ΔD the difference in distance between the position we have identified with the algorithm and the catalogued one. (**Emission properties section**) F_0 is the normalization flux ($MeV^{-1} cm^{-2} s^{-1}$); γ the spectral index; F the integrated photon flux from 30 GeV to 2 TeV ($ph\,cm^{-2}\,s^{-1}$) and N_{pred} the number of predicted photons in the model. Flux map and count map values are the normalized flux (x $4.37510^{11}\ ph\,cm^{-2}\,s^{-1}$) and the number of photons encounter in a specific position in our sky map. Bin1 goes from 30 GeV to 69 GeV; Bin2 from 69 GeV to 109 GeV: Bin3 from 109 GeV to 149 GeV: Bin4 from 149 GeV to 189 GeV and Bin5 from 189 GeV to 2 TeV. The pivot energy, E_b was fixed to 30 GeV. Finally we consider a source is variable if $Var > 24.72$.

Table 8. FSRQ Detectability

| | | | Detectability F/F_0 | | | | | | |
| | | | CTA | | | MAGIC | | | |
Source in 4FGL	ASSOC	z	5 h	15 h	50 h	5 h	15 h	50 h	$F_{max,est}$
J0348.6-2749	PKS0346-27	0.991	4.3	3.0	1.7	32.0	18.5	10.1	49.8
J0038.2-2459	PKS0035-252	1.196	28.8	27.3	15.0	290.1	167.5	91.7	26.9
J1422.5+3223	OQ334	0.682	10.6	5.9	3.2	58.5	33.8	18.5	63.1
J0028.5+2001	TXS0025+197	1.552	48.7	51.8	28.4	549.3	317.1	173.7	31.5
J0030.3-4224	PKS0027-426	0.495	23.1	12.9	7.0	118.4	68.3	37.4	2.4
J0222.0-1616	PKS0219-164	0.698	37.3	22.5	12.3	238.9	138.0	75.6	7.6
J2207.5-5346	PKS2204-54	1.215	61.3	44.2	24.2	468.6	270.5	148.2	3.3
J0505.8-0419	S30503-04	1.481	97.9	76.2	41.7	808.2	466.6	255.6	6.3
J0449.6-8100	PKS0454-81	0.444	103.2	65.5	35.9	694.9	401.2	219.8	10.6

Notes. Factor that the flux of a source has to reach, with respect to its quiescent state to be detected by CTA and MAGIC at different exposure times. $F_{max,est}$ is a rough estimation of the maximum flux reached by the source in the 12 years covered by 4FGL DR3. It is computed as max(Flux_History)/mean(Flux_History<mean(Flux_History)).

Table 9. BCU/Unknown Positions and Emission Properties

| | | | Position | | | Emission Properties | | | | | | | | | | | | | | |
| | | | | | | | | TS analysis results | | | | | Flux map | | | count map | | | | Var |
Source in 4FGL	ASSOC	TS	Ra [deg]	Dec [deg]	ΔD[deg]	F_0	$u(F_0)$	γ	$u(\gamma)$	F	u(F)	N_{pred}	Value	Total	Bin1	Bin2	Bin3	Bin4	Bin5	
J1416.1+1320	PKS B1413+135	110.08	214.03	13.35	0.059	1.56E-15	5.90E-16	2.13	0.44	2.56E-08	6.22E-08	21.34	4.06	5	3	1	1	0	0	1838.23
J0013.4+0950	1RXS J001328.4+094942	56.72	3.35	9.84	0.064	1.01E-15	4.97E-16	2.75	0.63	1.74E-11	5.91E-12	9.30	3.44	4	3	1	0	0	0	18.24
J2143.9+3337	MG3 J214351+3337	49.64	326.00	33.63	0.064	1.07E-15	5.07E-16	2.63	0.58	1.93E-11	6.17E-12	11.77	2.28	3	1	2	0	0	0	21.73
J0026.1-0732	-	46.30	6.54	-7.54	0.081	1.01E-15	6.68E-16	3.30	1.36	1.25E-11	5.30E-12	6.46	1.79	2	2	0	0	0	0	12.71
J1457.3-4246	PKS J1453-426	45.47	224.34	-42.78	0.014	8.49E-16	4.37E-16	2.58	0.59	1.61E-11	5.81E-12	8.83	4.18	5	3	2	0	0	0	437.67
J2359.9+3145	NVSS J235955+314558	38.11	359.99	31.76	0.027	1.10E-15	5.00E-16	5.00	0.00	6.87E-02	3.32E-02	4.91	2.37	3	3	0	0	0	0	17.28
J2226.6+0210	2MASS J22263636+0210373	37.76	336.66	2.17	0.189	4.16E-16	2.79E-16	1.90	0.64	1.25E-11	5.23E-12	6.52	1.77	2	1	1	0	0	0	20.61
J1158.8-1430	-	37.67	179.71	-14.50	0.021	4.30E-16	2.50E-16	1.69	0.47	9.61E-10	2.39E-09	8.23	1.76	2	1	1	0	0	0	5.70
J2210.8+3203	1RXS J221058.3+320327	35.86	332.72	32.05	0.034	3.83E-16	2.60E-16	2.17	0.62	9.66E-12	4.25E-12	5.78	2.32	3	2	0	1	0	0	14.95
J1324.5-2338	-	35.01	201.14	-23.64	0.076	1.11E-15	6.81E-16	3.94	1.32	1.13E-11	5.08E-12	6.08	1.71	2	2	0	0	0	0	16.67
J2241.3+2943	1RXS J224123.5+294244	33.99	340.34	29.72	0.030	5.82E-16	3.95E-16	2.80	0.97	9.49E-12	4.29E-12	5.59	2.36	3	1	2	0	0	0	25.36
J1039.6+0535	NVSS J103940+053608	32.30	159.91	5.59	0.024	4.62E-16	3.33E-16	2.51	0.82	9.08E-12	4.51E-12	4.76	1.76	2	1	1	0	0	0	6.65
J1249.3-0545	GALEXASC J124919.46-054539.7	30.83	192.33	-5.76	0.032	6.02E-16	4.39E-16	2.98	1.05	9.06E-12	4.42E-12	4.72	2.65	3	2	1	0	0	0	59.37
J1614.8-0850	1RXS J161443.4-085130	29.93	243.71	-8.84	0.036	1.04E-15	6.46E-16	3.23	1.09	1.40E-11	6.13E-12	7.66	2.51	3	2	1	0	0	0	12.67
J1428.7-1017	1RXS J142844.4-101801	29.13	217.20	-10.30	0.181	1.06E-15	7.52E-16	4.96	2.53	8.06E-12	4.30E-12	4.32	1.71	2	1	1	0	0	0	9.54
J1428.7-1017	1RXS J142844.4-101801	28.86	217.20	-10.30	0.047	1.06E-15	5.98E-16	4.99	1.19	8.01E-12	4.15E-12	4.29	2.57	3	3	0	0	0	0	9.54
J2207.1+2222	-	28.70	331.79	22.37	0.079	3.19E-16	2.45E-16	2.14	0.79	7.99E-12	4.02E-12	4.62	2.40	3	2	1	0	0	0	22.55
J1735.0-0132	1RXS J173502.6-013301	27.34	263.77	-1.55	0.050	9.14E-16	4.92E-16	5.00	0.00	6.85E-12	3.69E-12	3.85	2.46	3	3	0	0	0	0	4.74
J1646.7-1330	TXS 1644-133	24.84	251.70	-13.50	0.026	8.07E-16	5.21E-16	3.05	0.97	1.17E-11	5.33E-12	6.45	3.33	4	4	0	0	0	0	19.51
J0315.4-2643	NVSS J031527-264400	24.38	48.86	-26.73	0.061	1.38E-16	1.44E-16	1.44	0.97	5.68E-12	3.29E-12	3.18	2.47	3	1	2	0	0	0	12.52
J0415.2-5741	1RXS J041505.7-574237	23.80	63.80	-57.69	0.044	4.47E-16	3.26E-16	2.85	0.96	7.23E-12	3.71E-12	4.22	2.38	3	2	1	0	0	0	9.44
J1104.0+2611	SDSS J110357.29+261119.1	23.16	166.01	26.19	0.049	6.67E-16	4.93E-16	3.87	1.52	6.99E-12	3.65E-12	3.94	2.45	3	3	0	0	0	0	10.63
J1537.9-1344	1RXS J153757.1-134334	22.96	234.49	-13.73	0.027	5.80E-16	3.79E-16	2.52	0.70	1.14E-11	5.28E-12	6.18	2.53	3	2	1	0	0	0	14.86
J0011.8-3142	SUMSS J001141-314220	22.31	2.95	-31.72	0.022	3.33E-16	2.89E-16	2.33	1.27	6.81E-12	3.77E-12	3.63	2.60	3	3	0	0	0	0	24.59
J2041.1-6138	-	22.19	310.29	-61.64	0.037	1.36E-15	8.34E-16	4.59	1.52	1.14E-11	5.18E-12	6.12	1.72	2	2	0	0	0	0	8.43
J0030.9-3618	-	21.82	7.73	-36.31	0.059	3.79E-16	2.84E-16	2.48	0.82	7.64E-12	3.95E-12	4.13	1.71	2	1	1	0	0	0	17.84
J2057.6-7829	-	20.82	314.41	-78.49	0.286	5.94E-16	4.61E-16	3.42	1.34	7.38E-12	4.04E-12	3.89	1.76	2	2	0	0	0	0	12.16
J0705.9+5309	GB6 J0706+5309	19.31	106.49	53.17	0.092	4.12E-16	3.59E-16	2.96	1.65	5.99E-12	3.39E-12	3.70	2.23	3	3	0	0	0	0	15.82
J1514.4-7719	1RXS J151448.8-772249	19.13	228.61	-77.33	0.256	4.36E-16	3.26E-16	2.67	0.94	7.75E-12	4.02E-12	4.11	1.74	2	1	1	0	0	0	12.13
J0733.3-7615	-	18.86	113.35	-76.27	0.074	4.47E-16	3.61E-16	2.32	1.21	8.84E-12	4.52E-12	4.79	1.72	2	2	0	0	0	0	11.98
J0355.3+3909	CRATES J035515+390907	17.94	58.83	39.17	0.026	1.53E-16	1.43E-16	1.75	0.71	5.55E-12	3.31E-12	3.22	2.36	3	2	0	1	0	0	2.74
J0537.6+0400	-	17.68	84.42	4.00	0.042	7.86E-16	6.91E-16	4.32	2.18	7.10E-12	4.09E-12	3.79	1.72	2	2	0	0	0	0	12.51
J1017.2-1549	NVSS J101718-154933	17.08	154.32	-15.83	0.049	3.46E-16	2.93E-16	2.85	1.17	5.59E-12	3.31E-12	2.99	1.73	2	2	0	0	0	0	13.15
J1546.8-3244	-	16.22	236.72	-32.74	0.015	5.43E-16	4.57E-16	3.82	1.72	5.78E-12	3.42E-12	3.17	2.51	3	3	0	0	0	0	22.86

Notes. (**Position section**) Ra and Dec are the positions of the associated 4FGL source and ΔD the difference in distance between the position we have identified with the algorithm and the catalogued one. (**Emission properties section**) F_0 is the normalization flux ($MeV^{-1} cm^{-2} s^{-1}$); γ the spectral index; F the integrated photon flux from 30 GeV to 2 TeV ($ph\, cm^{-2}\, s^{-1}$) and N_{pred} the number of predicted photons in the model. Flux map and count map values are the normalized flux (x $4.37510^{11}\ ph\, cm^{-2}\, s^{-1}$) and the number of photons encounter in a specific position in our sky map. Bin1 goes from 30 GeV to 69 GeV; Bin2 from 69 GeV to 109 GeV: Bin3 from 109 GeV to 149 GeV: Bin4 from 149 GeV to 189 GeV and Bin5 from 189 GeV to 2 TeV. The pivot energy, E_b was fixed to 30 GeV. Finally we consider a source is variable if $Var > 24.72$.

Table 10. BCU/Unknown type Detectability

Source in 4FGL	ASSOC	z	CTA 5 h			CTA 15 h			CTA 50 h			MAGIC 5 h			MAGIC 15 h			MAGIC 50 h			$F_{max,est}$
			$z_{0.3}$	$z^*_{0.5}$	z_1	$z_{0.3}$	$z^*_{0.5}$	z_1	$z_{0.3}$	$z^*_{0.5}$	z_1	$z_{0.3}$	$z^*_{0.5}$	z_1	$z_{0.3}$	$z^*_{0.5}$	z_1	$z_{0.3}$	$z^*_{0.5}$	z_1	
J1416.1+1320	PKS B1413+135	0.247		1.5			0.8			0.4			8.6			5.0			2.7		22.2
J0013.4+0950	1RXS J001328.4+094942	-	7.9	9.4	14.5	4.3	5.2	8.8	2.3	2.9	4.8	39.5	48.6	93.1	22.8	28.0	53.8	12.5	15.4	29.4	5.7
J2143.9+3337	MG3 J214351+3337	-	6.1	7.6	12.4	3.3	4.2	7.5	1.8	2.3	4.1	31.5	38.7	79.7	18.2	22.3	46.0	9.9	12.2	25.2	5.9
J0026.1-0732		-	16.8	18.1	23.3	9.3	10.8	14.1	5.1	5.9	7.7	89.5	110.1	149.4	51.7	63.5	86.2	28.3	34.8	47.2	4.6
J1457.3-4246	PKS J1453-426	-	7.0	9.0	15.0	3.8	5.0	9.1	2.1	2.7	5.0	36.8	45.2	96.2	21.2	26.1	55.5	11.6	14.3	30.4	13.1
J2359.9+3145	NVSS J235955+314558	-	52.1	53.5	61.0	40.0	42.4	54.4	21.9	23.2	29.8	424.4	449.5	577.1	245.1	259.5	333.2	134.2	142.1	182.5	5.9
J2226.6+0210	2MASS J22263636+0210373	-	4.1	6.3	14.2	2.2	3.4	7.9	1.2	1.9	4.3	23.2	34.2	79.5	13.4	19.7	45.9	7.3	10.8	25.1	19.8
J1158.8-1430		-	2.5	4.2	10.4	1.3	2.3	5.8	0.7	1.3	3.2	14.9	24.3	56.5	8.6	14.0	32.6	4.7	7.7	17.9	3.7
J2210.8+3203	1RXS J221058.3+320327	-	7.7	11.0	21.9	4.2	6.0	12.2	2.3	3.3	6.7	42.8	55.4	128.9	24.7	32.0	74.4	13.5	17.5	40.8	17.9
J1324.5-2338		-	26.7	28.3	35.2	16.2	17.1	22.0	8.8	9.4	12.0	171.4	181.5	233.0	98.9	104.8	134.5	54.2	57.4	73.7	6.6
J2241.3+2943	1RXS J224123.5+294244	-	15.10	17.6	26.5	8.2	9.8	16.0	4.5	5.4	8.8	74.7	91.9	169.9	43.1	53.1	98.1	23.6	29.1	53.7	9.7
J1039.6+0535	NVSS J103940+053608	-	11.5	15.2	26.1	6.2	8.5	15.7	3.4	4.6	8.6	61.6	75.7	167.4	35.5	43.7	96.7	19.5	23.9	52.9	3.5
J1249.3-0545	GALEXASC J124919.46-054539.7	-	18.6	21.5	29.8	10.3	12.0	18.0	5.7	6.6	9.9	94.0	115.6	191.2	54.3	66.8	110.4	29.7	36.6	60.5	4.8
J1614.8-0850	1RXS J161443.4-085130	-	14.9	16.6	21.3	8.3	9.6	12.9	4.5	5.3	7.1	78.6	96.7	136.9	45.4	55.8	79.0	24.9	30.6	43.3	12.5
J1428.7-1017	1RXS J142844.4-101801	-	52.8	54.3	61.9	40.0	42.3	54.4	21.9	23.2	29.8	424.2	449.2	576.8	244.9	259.3	333.0	134.1	142.1	182.4	3.9
J1428.7-1017	1RXS J142844.4-101801	-	53.7	55.2	62.9	41.1	43.5	55.9	22.5	23.8	30.6	436.0	461.7	592.8	251.7	266.5	342.2	137.9	146.0	187.4	3.9
J2207.1+2222		-	8.7	12.5	25.2	4.7	6.8	14.0	2.6	3.7	7.7	48.1	63.3	147.3	27.8	36.6	85.0	15.2	20.0	46.6	30.2
J1735.0-0132	1RXS J173502.6-013301	-	62.7	64.4	73.5	48.2	51.0	65.5	26.4	27.9	35.9	510.8	540.9	694.5	294.9	312.3	401.0	161.5	171.1	219.6	5.5
J1646.7-1330	TXS 1644-133	-	15.1	17.4	23.5	8.4	9.7	14.2	4.6	5.3	7.8	77.0	94.7	150.6	44.5	54.7	86.9	24.4	30.0	47.6	32.1
J0315.4-2643	NVSS J031527-264400	-	4.6	8.5	23.3	2.4	4.6	13.0	1.3	2.5	7.1	25.8	48.2	121.2	14.9	27.8	70.0	8.1	15.2	38.3	4.2
J0415.2-5741	1RXS J041505.7-574237	-	21.0	24.3	35.8	11.6	13.5	21.7	6.3	7.4	11.9	104.0	128.0	229.9	60.1	73.9	132.7	32.9	40.5	72.7	22.0
J1104.0+2611	SDSS J110357.29+261119.1	0.712		48.4			29.2			16.0			310.1			179.0			98.1		3.3
J1537.9-1344	1RXS J153757.1-134334	-	9.2	12.2	20.8	5.0	6.8	12.6	2.7	3.7	6.9	49.2	60.5	133.7	28.4	34.9	77.2	15.6	19.1	42.3	16.4
J0011.8-3142	SUMSS J001141-314220	-	11.7	16.7	31.0	6.3	9.0	17.2	3.5	4.9	9.4	65.4	80.4	186.9	37.7	46.4	107.9	20.7	25.4	59.1	19.7
J2041.1-6138		-	34.1	35.0	40.0	22.8	24.2	31.0	12.5	13.2	17.0	242.0	256.2	329.0	139.7	147.9	189.9	76.5	81.0	104.0	2.4
J0030.9-3618		-	13.2	17.7	30.9	7.2	9.9	18.3	3.9	5.4	10.0	71.2	87.6	198.0	41.1	50.6	114.3	22.5	27.7	62.6	12.0
J2057.6-7829		-	32.1	34.0	43.7	18.4	20.6	26.4	10.1	11.3	14.5	180.3	218.2	280.2	104.1	126.0	161.8	57.0	69.0	88.6	12.0
J0705.9+5309	GB6 J0706+5309	-	26.4	30.5	42.8	14.7	17.0	25.9	8.0	9.3	14.2	133.0	163.6	274.2	76.8	94.4	158.3	42.1	51.7	86.7	4.8
J1514.4-7719	1RXS J151448.8-772249	-	16.1	19.9	31.7	8.7	11.0	19.2	4.8	6.1	10.5	82.5	101.5	203.2	47.6	58.6	117.3	26.1	32.1	64.3	20.2
J0733.3-7615		-	8.4	12.1	22.6	4.6	6.5	12.6	2.5	3.6	6.9	47.6	58.5	136.0	27.5	33.8	78.5	15.0	18.5	43.0	14.3
J0355.3+3909	CRATES J035515+390907	-	8.1	13.3	31.8	4.3	7.2	17.7	2.4	4.0	9.7	47.4	75.0	174.5	27.4	43.3	100.7	15.0	23.7	55.2	3.7
J0537.6+0400		-	51.6	53.0	60.5	31.6	33.5	43.0	17.3	18.3	23.5	335.3	355.1	455.9	193.6	205.0	263.2	106.0	112.3	144.2	5.8
J1017.2-1549	NVSS J101718-154933	-	27.2	31.4	46.3	14.9	17.5	28.0	8.2	9.6	15.3	134.3	165.2	296.9	77.6	95.4	171.4	42.5	52.2	93.9	30.0
J1546.8-3244		-	49.2	52.1	66.9	29.70	31.5	40.4	16.3	17.3	22.1	315.5	334.1	429.0	182.2	192.9	247.7	99.8	105.7	135.7	7.1

Notes. Factor that the flux of a source has to reach, with respect to its quiescent state to be detected by CTA and MAGIC at different exposure times and for different redshifts. In case the redshift is measured we only show the value of the factor for that specific z in the column $z^*_{0.5}$, the remaining values in $z_{0.3}$ and z_1 are empty. $F_{max,est}$ is a rough estimation of the maximum flux reached by the source in the 12 years covered by 4FGL DR3. It is computed as max(Flux_History)/mean(Flux_History<mean(Flux_History)).

Table 11. New Sources Positions and Emission Properties

| | | | Position | | | Emission Properties | | | | | | | | | | | | | |
| | | | | | | TS analysis results | | | | | | | Flux map | count map | | | | | |
Source	Possible ASSOC	TS	Ra [deg]	Dec [deg]	$\Delta D[deg]$	F_0	$u(F_0)$	γ	$u(\gamma)$	F	u(F)	N_{pred}	Value	Total	Bin1	Bin2	Bin3	Bin4	Bin5
941	PKS 1351+021	30.6	208.49	1.87	0.024	3.52E-16	2.78E-16	2.26	0.99	7.73E-12	3.91E-12	4.15	1.71	2	2	0	0	0	0

Notes. (**Position section**) Ra and Dec are the positions of the possible associated source and ΔD the difference in distance between the position we have identified with the algorithm and the catalogued one. (**Emission properties section**) F_0 is the normalization flux ($MeV^{-1}cm^{-2}s^{-1}$); γ the spectral index; F the integrated photon flux from 30 GeV to 2 TeV ($ph\,cm^{-2}\,s^{-1}$) and N_{pred} the number of predicted photons in the model. Flux map and count map values are the normalized flux (x $4.37510^{11}\ ph\,cm^{-2}\,s^{-1}$) and the number of photons encounter in a specific position in our sky map. Bin1 goes from 30 GeV to 69 GeV; Bin2 from 69 GeV to 109 GeV: Bin3 from 109 GeV to 149 GeV: Bin4 from 149 GeV to 189 GeV and Bin5 from 189 GeV to 2 TeV. The pivot energy, E_b was fixed to 30 GeV.

Table 12. New Sources Detectability

| | | | Detectability F/F_0 | | | | | |
| | | | CTA | | | MAGIC | | |
Source id	ASSOC	z	5 h	15 h	50 h	5 h	15 h	50 h
941	PKS 1351+021	1.608	41.0	24.8	13.6	262.9	151.8	83.1

Notes. Factor that the flux of the source has to reach, with respect to its quiescent state to be detected by CTA and MAGIC at different exposure times.

5. Conclusions

Throughout this work we have analysed almost 13 years of *Fermi*-LAT data with the aim of expanding the current family of VHE sources that can be followed-up by IACTs. We started by building a skymap suitable for our scientific case using the fermitools. We then implemented a source detection algorithm used to identify photon clusters in the skymap and perform a spatial association with sources catalogued by *Fermi*-LAT. In this step, we have discarded the ones already included in the 3FHL/2FHL catalogs. We filtered the remaining ones through a statistical test and a TS map when necessary. Finally we studied their detectability with CTA and MAGIC.

From the initial 1741 seeds, a subsample of 389 were analysed with the outcome of some interesting candidates. For BLLs we have 3 possible candidates to be detected with CTA in 5 h: J1637.7+7326, J0135.1+0255 and J0033.3-2040; whereas for EXTs we have 9: J1544.3-0649, J1348.9+0756, J0830.0+5231, J1215.1+0731, J1310.6+2449, J2321.0-6308, J2201.9-1706, J0303.3+0555 and J2202.7-5637. In the case of FSRQs, the source J0038.2-2459 can be detected by CTA in 15 h and finally a 'New Source' has been observed although with a so far unclear association.

Future work could be to analyse the 1352 remaining seeds, some of which have photons in the higher energy bins, in search of more EXT or FSRQ candidates. We could also study the light curves of the most promising objects with the aim of having a more accurate idea of the fluxes they can reach. However, the most interesting follow up would be to study in more depth the 'New Source' given its unusual nature.

In any case, what is clear is that gamma rays are destined to play a crucial role in the exploration of non-thermal phenomena in the Universe and expanding the VHE family of sources offers us an unique opportunity to delve deeper into the physics of extreme environments. Investigating the correlations between activity in the gamma-ray band and other wavelengths; testing the possible link with high-energy neutrinos sources or study the extragalactic background light are some of the wide variety of possibilities. The gamma-ray window has been opened and we have only begun to look out.

References

[1] Nievas Rosillo, M. (2018). Observations of VHE emission from blazars at cosmological distances.

[2] Rosillo, M. N., Domínguez, A., Chiaro, G., La Mura, G., Brill, A., Paliya, V. S. (2021). Hunting extreme BL Lacertae blazars with Fermi-LAT. Monthly Notices of the Royal Astronomical Society.

[3] Hickox, R. C., Alexander, D. M. (2018). Obscured active galactic nuclei. arXiv preprint arXiv:1806.04680.

[4] Meyers, R. A. (2002). Encyclopedia of physical science and technology. Academic.

[5] Prince, R. (2020). Multi-wavelength Data Analysis and Theoretical Modeling of Blazar Flares (Doctoral dissertation, Raman Research Institute, Bangalore).

[6] Ghisellini, G., Righi, C., Costamante, L., Tavecchio, F. (2017). The Fermi blazar sequence. Monthly Notices of the Royal Astronomical Society, 469(1), 255-266.

[7] Nandikotkur, G., Jahoda, K. M., Hartman, R. C., Mukherjee, R., Sreekumar, P., Boettcher, M., ... Swank, J. H. (2006). Does the Blazar Gamma-ray Spectrum Harden with Increasing Flux?-Analysis of Nine Years of EGRET Data. AAS/High Energy Astrophysics Division 9, 9, 7-47.

[8] Padovani, P. (2017). Active galactic nuclei at all wavelengths and from all angles. Frontiers in Astronomy and Space Sciences, 4, 35.

[9] Cooray, A. (2016). Extragalactic background light measurements and applications. Royal Society Open Science, 3(3), 150555.

[10] Aharonian, F., Buckley, J., Kifune, T., Sinnis, G. (2008). High energy astrophysics with ground-based gamma ray detectors. Reports on Progress in Physics, 71(9), 096901.

[11] `https://fermi.gsfc.nasa.gov/ssc/data/analysis/documentation/Cicerone/Cicerone_Introduction/LAT_overview.html`

[12] Radiación de Cherenkov. (2022, 25 de septiembre). Wikipedia, La enciclopedia libre. Fecha de consulta: 15:45, noviembre 28, 2022 desde `https://es.wikipedia.org/wiki/Radiacion_de_Cherenkov`

[13] Sitarek, J. (2022). TeV Instrumentation: current and future. Galaxies, 10(1), 21.

[14] Graña González, A. (2021). Desarrollo de una estrategia de observación de características espectrales en blázares con CTA.

[15] `https://fermi.gsfc.nasa.gov/cgi-bin/ssc/LAT/LATDataQuery.cgi`

[16] Longair, M. S. (2010). *High energy astrophysics*. Cambridge University Press.

[17] Ackermann, M., Ajello, M., Atwood, W. B., Baldini, L., Ballet, J., Barbiellini, G., ... Wood, K. S. (2016). 2FHL: the second catalog of hard Fermi-LAT sources. The Astrophysical Journal Supplement Series, 222(1), 5.

[18] Mattox, J. R., Bertsch, D. L., Chiang, J., Dingus, B. L., Digel, S. W., Esposito, J. A., ... Willis, T. D. (1996). The likelihood analysis of EGRET data. The Astrophysical Journal, 461, 396.

[19] `https://fermi.gsfc.nasa.gov/ssc/data/analysis/documentation/Cicerone/Cicerone_Likelihood/Likelihood_overview.html`

[20] `https://fermi.gsfc.nasa.gov/ssc/data/analysis/user/`

[21] `https://tools.ssdc.asi.it/`

[22] Willis, T. D. (1996). The likelihood analysis of EGRET data. The Astrophysical Journal, 461, 396.

[23] `https://raw.githubusercontent.com/fermi-lat/fermitools-fhelp/master/fhelp_files/gtdiffrsp.txt`

[24] `https://fermi.gsfc.nasa.gov/ssc/data/analysis/documentation/Cicerone/Cicerone_Likelihood/Fitting_Models.html`

[25] Abdo, A. A., Ackermann, M., Ajello, M., Atwood, W. B., Axelsson, M., Baldini, L., ... Raino, S. (2009). Fermi/large area telescope bright gamma-ray source list. The Astrophysical Journal Supplement Series, 183(1), 46.

[26] Ackermann, M., Ajello, M., Allafort, A., Antolini, E., Atwood, W. B., Axelsson, M., ... Spandre, G. (2011). The second catalog of active galactic nuclei detected by the Fermi Large Area Telescope. The Astrophysical Journal, 743(2), 171.

[27] `https://fermi.gsfc.nasa.gov/ssc/data/analysis/documentation/Cicerone/`

[28] Shahinyan, K. (2017). The State of the Blazar: Investigations of Variability Patterns in the Very High Energy Gamma-ray Emission from Northern Blazars.

[29] Ajello, M., Atwood, W. B., Baldini, L., Ballet, J., Barbiellini, G., Bastieri, D., ... Wood, M. (2017). 3FHL: The third catalog of hard Fermi-LAT sources. The Astrophysical Journal Supplement Series, 232(2), 18.

[30] Prandini, E., Ghisellini, G. (2022). The Blazar Sequence and Its Physical Understanding. Galaxies, 10(1), 35.

[31] `https://fermi.gsfc.nasa.gov/ssc/data/analysis/scitools/`

[32] Dominguez, A., Primack, J. R., Rosario, D. J., Prada, F., Gilmore, R. C., Faber, S. M., ... Cooper, M. C. (2011). Extragalactic background light inferred from AEGIS galaxy-SED-type fractions. Monthly Notices of the Royal Astronomical Society, 410(4), 2556-2578.

[33] `http://tevcat.uchicago.edu/`

March 2023
San Cristóbal de La Laguna

Universidad
de La Laguna